Investigation of processes controlling summertime gaseous elemental mercury oxidation at mid-latitudinal marine, coastal, and inland Sites

Zhuyun Ye[1], Huiting Mao[1], Che-Jen Lin[2,3], and Su Youn Kim[4]

[1] Department of Chemistry, State University of New York College of Environmental Science and Forestry, Syracuse, NY, 13210, USA

[2] Center for Advances in Water and Air Quality, Lamar University, Beaumont, TX, 77710, USA

[3] Department of Civil and Environmental Engineering, Lamar University, Beaumont, TX, 77710, USA

[4] R&D Program Evaluation Division Office of National Evaluation and Analysis Korea Institute of S&T Evaluation and Planning (KISTEP), Seoul, South Korea

Received: 13 October 2015 – Accepted: 23 October 2015 – Published: 15 January 2016

Correspondence to: Z. Ye (zye01@syr.edu)

Abstract

A box model incorporating a state-of-the-art chemical mechanism for atmospheric mercury (Hg) cycling was developed to investigate oxidation of gaseous elemental mercury (GEM) at three locations in the northeastern United States: Appledore Island (marine), Thompson Farm (coastal, rural), and Pack Monadnock (inland, rural, elevated). The chemical mechanism in this box model included the most up-to-date Hg and halogen chemistry. As a result, the box model was able to simulate reasonably the observed diurnal cycles of gaseous oxidized mercury (GOM) and chemical speciation bearing distinct differences between the three sites. In agreement with observations, simulated GOM diurnal cycles at AI and TF showed significant daytime peaks in the afternoon and nighttime minimums compared to flat GOM diurnal cycles at PM. Moreover, and significant differences in magnitude of GOM diurnal amplitude (AI>TF>PM) were captured in modeled results. At the coastal and inland sites, GEM oxidation was predominated by O_3 and OH, contributing 80–99% of total GOM production during daytime. H_2O_2 initiated GEM oxidation was significant (~33% of the total GOM) at the inland site during nighttime. In the marine boundary layer (MBL) atmosphere, Br and BrO became dominant GEM oxidants with mixing ratios reaching 0.1 and 1 pptv, respectively, contributing ~70% of the total GOM production during mid-day, while O_3 dominated GEM oxidation (50–90% of GOM production) over the remaining day when Br and BrO mixing ratios were diminished. The majority of HgBr produced from GEM+Br was oxidized by NO_2 and HO_2 to form brominated GOM species. Relative humidity and products of the CH_3O_2+BrO reaction possibly affected significantly the mixing ratios of Br or BrO radicals and subsequently GOM formation. Gas-particle partitioning could be potentially important in the production of GOM as well as Br and BrO at the marine site.

1 Introduction

Mercury (Hg) is a toxic pollutant found globally in air, natural waters, and soils. The health concern of Hg arises from the neurotoxic organic form, methyl mercury (MeHg), in the aquatic environments (Mason et al., 2006; Miller et al., 2007; Rolfhus et al., 2003). The high bioaccumulation and biomagnification of MeHg lead to human exposure through the consumption of seafood (Clarkson, 1994). Deposition of atmospheric Hg is one of the most important sources of aquatic Hg.

In the atmosphere, Hg exists in three forms: gaseous elemental mercury (GEM), gaseous oxidized mercury (GOM), and particulate bound mercury (PBM). The majority of atmospheric Hg is GEM, comprising > 95% of total gaseous mercury (TGM=GEM+GOM). The 0.8–1.7 years atmospheric lifetime of GEM is conducive to long range transport of Hg as a global pollutant (Bergan et al., 1999; Bergan and Rodhe, 2001; Holmes et al., 2006; Lin and Pehkonen, 1999; Schroeder and Munthe, 1998; Selin et al., 2007). In contrast, GOM and PBM are relatively short-lived and subject to wet deposition and stronger dry deposition than GEM due to their high solubility in water and low vapor pressure. GOM in the atmosphere can be produced from oxidation of GEM, released directly from anthropogenic emissions, and transformed from PBM. In remote regions, in-situ GOM production may be the major source of GOM (Weiss-Penzias et al., 2003; Poissant et al., 2004; Mao and Talbot, 2012) considering its short lifetime.

Chemical speciation of atmospheric Hg is essential to understand its geochemical cycle. Theoretical and experimental studies suggested that the main oxidants of GEM in the atmosphere are ozone (O_3), hydroxyl radical (OH), atomic bromine (Br), bromine monoxide (BrO), hydrogen peroxide (H_2O_2), and atomic chlorine (Cl), yielding GOM species of HgO, HgBrO, HgBr, $Hg(OH)_2$, HgCl, and through further reaction to other mercury halides (Ariya et al., 2015; Dibble

59   et al., 2012; Lin and Pehkonen, 1999). Although efforts have been made to investigate the relative

60   importance of these oxidants for GEM oxidation in the troposphere, it is still not well understood.

61   In the terrestrial environment, it was suggested that the oxidation of GEM was primarily by O_3 and

62   OH radicals (Shon et al., 2005; Sillman et al., 2007). The speciation and quantification of GEM +

63   O_3 product(s) still remain unknown and debatable (Ariya et al., 2015; Gustin et al., 2013; Rutter

64   et al., 2012). An experimental study by Pal and Ariya (2004b) measured 1% of HgO produced by

65   GEM + O_3 on an aerosol filter. Snider et al. (2008) showed HgO(s) production in their kinetic and

66   product study. Schroeder et al. (1998) suggested HgO would not exist as an isolated molecule in

67   gas phase but could be deposited to and retained by manifold given a decomposition temperature

68   of +500 °C. However, the GEM + O_3 reaction and decomposition temperature (Schroeder et al.,

69   1998) could also be impacted by the presence of other ambient gases (Snider et al., 2008; Gustin

70   et al., 2013; Seigneur et al., 1994). A recent study of Huang et al. (2013) observed gas-phase HgO

71   using nylon and cation exchange membranes. The reaction of GEM+OH has been subject to debate

72   between theoretical and experimental studies, as no mechanism consistent with thermochemistry

73   has been proposed (Ariya et al., 2015; Pal and Ariya, 2004a; Subir et al., 2011). Measurement

74   studies on GOM in polar regions (Simpson et al., 2007; Steffen et al., 2008) and sub-tropical MBL

75   (Laurier et al., 2003; Laurier and Mason, 2007; Obrist et al., 2011) as well as atmospheric modeling

76   studies on mercury cycling (Holmes et al., 2009, 2010; Kim et al., 2010; Lindberg et al., 2002;

77   Obrist et al., 2011; Soerensen et al., 2010; Toyota et al., 2014; Wang et al., 2014; Xie et al., 2008)

78   have suggested Br as an important oxidant of GEM. The major source of atmospheric Br was

79   suggested to be produced photolytically from Br-containing compounds and through the Br/BrO

80   cycle involving tropospheric O_3 (Saiz-Lopez and Glasow, 2012; Simpson et al., 2015).

81   GOM concentrations and speciation could be impacted by meteorological conditions and

82   chemical conditions in different environments. High solubility of GOM species, possible phase

83   partitioning of HgO as discussed above could all be the reasons causing varying GOM speciation

84   at different locations. For instance, the aerosol type, size distribution, and chemical composition

85   varied largely between the MBL site and inland sites, which may lead to different gas-particle

86   partitioning rates of GOM species.

87   Hg chemistry in the MBL, the lowest part of the troposphere in direct contact with the sea

88   surface, has global importance as approximately 70% of the earth's surface is covered by oceans

89   (Glasow et al., 2002). Hg in the MBL cycles differently from in coastal or inland areas. However,

90   contemporary models are not able to reproduce GOM observations temporally and spatially due

91   to knowledge gaps in Hg science, simplified model assumptions, and uncertainties of

92   measurements (Ariya et al., 2015; Lin et al., 2006). In the polar region, bromine radicals were

93   identified as the primary cause of the Arctic mercury depletion events (AMDE) (Kim et al., 2010;

94   Lindberg et al., 2002; Toyota et al., 2014; Xie et al., 2008). In the MBL outside Polar Regions,

95   due to lower mixing ratios of atmospheric halogen radicals, often lower than the detection limit,

96   mechanisms for GOM production were more controversial than in Polar Regions. Using a box

97   model, Hedgecock et al. (Hedgecock et al., 2003; Hedgecock and Pirrone, 2004, 2005) suggested

98   that O_3 was a dominant GEM oxidant in the MBL at mid-latitudes in the Mediterranean region,

99   and that the GEM+O_3 reaction may form solid products. However, the reaction kinetics in their

100   model were out-of-date with limited halogen chemistry, and fixed emissions used in the model

101   oversimplified the source terms. Holmes et al. (2009) simulated that GEM oxidation by Br

102   comprised 35–60% of the GOM sources using BrO concentrations calculated at a photostationary

103   state from a prescribed distribution of Br mixing ratios. Additionally, a parameter was introduced

104   in the same study to account for entrainment of free tropospheric GOM into the MBL and the Br

105   mixing ratio was adjusted to capture the observed GOM diurnal trend, which could cause large

106   uncertainties in GOM simulations. Most recently, Wang et al. (2014) employed updated Hg

107   reactions together with bromine and iodine reactions, adopting the free tropospheric GOM

108   entrainment parameter from Holmes et al. (2009) for tropical MBL, and found Br to be a primary

109   GEM oxidant, but oxidation by Br or O_3/OH alone was unable to reproduce observed GOM

110   concentration. However, different GEM oxidants could be dominant in different environments, as

111   a result of the unique composition and concentration levels of in-situ oxidants those environments

112   may be characterized with.

113   In this study, we employed a state-of-the-art chemical mechanism that incorporates gas and

114   aqueous phase chemistry of Hg, O_3, and halogen to investigate the dynamics of GOM formation

115   under various atmospheric conditions in mid-latitude regions. The most up-to-date kinetics was

116   applied. Halogen radical mixing ratios (such as Br and BrO) were calculated using up-to-date

117   atmospheric halogen reactions. Clear sky days with calm wind conditions were selected, which are

118   mostly associated with strong atmospheric stability, to minimize the entrainment effect of free

119   tropospheric air and regional transport and hence no entrainment factor was included in this study.

120   Moreover, the initial GEM mixing ratios along with a list of compounds (Table 2) in the model

121   were obtained from observations in three different environments and were set to be constant during

122   simulations. Fixing the input concentrations of GEM among a number of other compounds (Table

123   2) as constants using observational data enabled a modeled chemical environment close to the real

124   atmospheric environment that is being studied.   Moreover, a box model simulates the

125   concentrations of short-lived compounds reaching an instantaneous chemical steady state, and for

126   the time scales of such instants, the chemicals such as GEM are long-lived enough to maintain a

127 constant level. In Section 2, the methods employed were laid out in detail. Section 3 presented

128 results of reasonably simulated differences between GOM diurnal cycles at the three locations that

129 were captured in measurement data, major GEM oxidants in the three environments, and a detailed

130 discussion of the sensitivity of physical parameters and important chemical reactions. Section 4

131 summarized the key findings and implications from this study.

2 Methods

2.1 Box Model Description

134   The Kinetic PreProcessor version 2.1 (Sandu and Sander, 2006) was utilized as the

135 framework of the box model (Hedgecock et al., 2003; Hedgecock and Pirrone, 2004, 2005). A

136 second order Rosenbrock method (Verwer et al., 1999) was applied to solve the coupled ordinary

137 differential equations. The box model used in this study was initially set up by Kim et al. (2010).

138 It was further improved in this study by incorporating the most up-to-date gas and aqueous phase

139 chemical mechanisms (Atkinson et al., 2004, 2008; Dibble et al., 2012; Sander et al., 2011) to the

140 model.

141 2.1.1   Reactions and kinetics

142   The box model has a total of 424 reactions: 276 gas-phase reactions (including Hg, halogen,

143 O_3, sulfate, and hydrocarbon reactions), 52 gas-water equilibriums, 28 aqueous equilibriums and

144 68 aqueous reactions. Most of these reactions and kinetic data were updated based on JPL Report

145 No. 17 (Sander et al., 2011), the halogen chemistry reviews of Atkinson et al. (2004, 2008), and

146 the references listed in Table 1. Photodissociation coefficients were calculated from the

147 Tropospheric Ultraviolet and Visible (TUV) Radiation Model (Madronich, 1993).

148   The most important improvements in chemistry are gas and aerosol phase of Hg and

149 halogen reactions. Gas-phase Hg reactions included in the box model are (Table 1):

150   1. Oxidation of GEM by O_3, OH, H_2O_2, Br, BrO, Cl, Cl_2, I (G1–8);

151   2. Reduction of HgBr and HgI to produce GEM (G9–11); and

152   3. Reactions of HgBr/HgCl with BrO, ClO, IO, NO_2, HO_2, and OH (G12–24) with kinetics

153 suggested by Dibble et al. (2012).

154   Aqueous Hg reactions include (Table S1):

155   1. Oxidations of Hg by O_3, OH, HOCl, and ClO^-, further oxidation of HgOH by O_2;

156   2. Reduction of Hg^{2+} by HO_2, photolytic reduction of $Hg(OH)_2$ and S(IV)-mediated

157 reduction; and

158   3. Aqueous equilibria involving $HgSO_3$, $Hg(SO_3)_2^{2-}$, $HgOH^+$ and $Hg(OH)_2$. Gasphase

159 halogen reactions in the box model are mainly cycles of halogen radicals (Cl/Br/I and ClO/BrO/IO

160 radicals).

161   The Cl/Br/I radical cycles include photodissociation of Cl_2/Br_2/I_2, organic halides, and

162 other inorganic halides as sources, and oxidation reactions as sinks. The ClO/BrO/IO radical cycles

163 involve oxidation of Cl/Br/I radicals, photodissociation of $ClNO_2$/$ClONO_2$/$BrNO_2$/$BrONO_2$,

164 production from other halogen radicals, and sink reactions to calculate Cl/Br/I radicals or other

165 halides. Aqueous halogen reactions include reactions of Br^-/Cl^- and reactions of aqueous BrCl,

166 HCl, HBr, HOCl, HOBr, Cl_2, and Br_2 species. The chemistry of halogen radicals, especially the

167 reaction cycles of Br and BrO radicals, could be important and should not be neglected or replaced

168 by simple approximation. Hence, the most up-to-date halogen chemistry from the literature was

169 included in our model.

170 2.1.2   Initial conditions and input data

171   Observations at three sites from the University of New Hampshire (UNH) AIRMAP

172 Observing Network (http://www.eos.unh.edu/observatories/data.shtml) were used: a marine site

173 located on Appledore Island (AI) at the Shoals Marine Lab, the Gulf of Maine (42.97°N, 70.62°W,

174 40 m a.s.l.), a coastal site located in Thompson Farm (TF) in Durham, NH (43.11°N, 70.95°W, 24

175 m a.s.l.) and 25 km away from the Gulf of Maine, and a forested 90 km inland site located on Pack

176 Monadnock (PM) in Miller State Park in Peterborough, NH (42.86°N, 71.88°W, 700 m a.s.l.) (Fig.

177 1). Hourly mean values of GEM, O_3, CO, NO, meteorological observations (i.e., temperature,

178 relative humidity, and solar radiation) at these three sites were used as initial input to the box model.

179 For species that were not measured, we set their initial concentrations as the values in similar

180 environments from the literature if available. Observations of GOM mixing ratios from the three

181 sites were utilized to evaluate the model performance. GEM and GOM data were collected using

182 the Tekran® 2537/1130/1135 speciation unit (Tekran Inc., Canada). For these three sites, the

183 instruments were first run and calibrated in the laboratory and then operated at the sites in a

184 consistent manner. GEM was measured at 5-min intervals and with a limit of detection (LOD) of

185 ~5-10 ppqv (Mao et al., 2008), GOM was measured over a 2-h sampling period with a LOD of

186 ~0.1 ppqv based on three times the standard deviation of the field blank values (Sigler et al., 2009;

187 Mao and Talbot, 2012). A custom-built refrigerator assembly and a canister of drierite was used

188 to cool and dry air streams before entering into the 1130 pump module, resulting in < 25% RH of

189 air streams (Sigler et al., 2009). Detailed information on these measurements can be found in Mao

190 and Talbot (2004; 2012), Talbot et al. (2005), Fischer et al. (2007), Mao et al. (2008), and Sigler

191 et al. (2009). Table 2 lists the input variables of the box model. The model's initial mixing ratios

192 of GEM, O_3, CO, and NO were obtained from observations and were set to be constant during

193 each 1h simulation. Br/Cl/I concentrations were all calculated from the model given initial

194 concentrations of 1 pptv (Finley et al., 2008; except for AI) for Br_2, Cl_2, and I_2 species. At AI, the

195 Br_2 initial concentration was set to be constant during simulations and used Saiz-Lopez et al.

196   (2006)'s values to constrain [BrO]. Detailed information can be found in Section 3.3.1. Dry

197   deposition flux was calculated using dry deposition velocity data derived from Zhang et al. (2009,

198   2012) and boundary layer height estimated from Mao and Talbot (2004). Other physical

199   parameters (i.e. Henry's constants, liquid water content, and aerosol radius) were used to simulate

200   the gas-particle partitioning process in the box model.

201   2.1.3   Gas-particle partitioning

202   An empirical expression was utilized to calculate particle size growth relative to its dry

203   radius (r_{dry}) (Lewis and Schwartz, 2006):

204    $$r = r_{dry} \frac{4}{3.7} \left(\frac{2-RH}{1-RH} \right)^{1/3},$$ (1)

205   where RH is the relative humidity, and r is the particle radius at RH.

206   Gas-particle partitioning was treated by mass transfer between droplets and air. The

207   dynamic mass transfer coefficient across the gas-aqueous interface was calculated using the

208   method developed by Schwartz (1986). The net mass flux (F, molecule cm^{-3} s^{-1}) between the gas

209   and aqueous phase is given by

210    $$F = k_{mt} \times \left(L \times c_g - \frac{c_{aq}}{HRT} \right),$$ (2)

211   where L is the liquid water content ($m^3_{water} m^{-3}_{air}$), k_{mt} is the mass transfer coefficient (s^{-1}), c_g is the

212   gas phase concentration of the species (molecules cm^{-3}), c_{aq} is the aqueous phase concentration of

213   species (molecules cm^{-3}), H is the Henry's constant of the species (M atm^{-1}), R is the universal gas

214   constant (atm L K^{-1} mol^{-1}), and T is atmospheric temperature (K). k_{mt} is calculated as follow:

215    $$k_{mt} = \left(\frac{r^2}{3D_g} + \frac{4r}{3\overline{v}\alpha} \right)^{-1},$$ (3)

216    $$\overline{v} = (8RT/M\pi)^{1/2},$$ (4)

217   where r is the particle radius (μm), D_g is the diffusion coefficient ($m^2 s^{-1}$), $\bar{v}$ is the mean thermal

218   molecular velocity (m s^{-1}), α is the dimensionless accommodation coefficient, and M is the species

219   molecular weight (g mol^{-1}).

220   **2.2   Case Selection**

221   A total of 83 cases were examined to investigate the role of chemistry in Hg cycling in the

222   MBL, coastal, and inland environments. At the study sites, significant warm season declines of

223   GEM were observed with annual maximums in spring and minimums in autumn resulting in

224   seasonal amplitudes up to 100 ppqv at TF (Mao et al., 2008). The lost GEM during the warm

225   season most likely entered the ecosystem. Chemical transformation of GEM in warm seasons was

226   suspected to be one of the factors causing the observed seasonal decline in GEM. As such, this

227   study selected the cases representing summer days when chemical processes were most likely

228   dominant. To exclude the influence of wet deposition, we selected clear-sky conditions based on

229   the observed photodissociation rate constant of NO_2 (jNO_2) and solar radiation flux. To minimize

230   the influence of transport, cases with arithmetic daily mean wind speed higher than 75% percentile

231   of all summer days in studied years (> 1.3 m s^{-1} at TF, > 6 m s^{-1} at PM, and > 7 m s^{-1} at AI) were

232   excluded. As a result, 50, 12, and 21 clear-sky days at AI (marine), TF (coastal), and PM (inland,

233   elevated), respectively, were selected from summers of 2007, 2008, and 2010. Since there was no

234   temperature data available for summer 2009 at TF, 2009 was not considered.

235   **2.3   Backward Trajectory Model**

236   The National Oceanic and Atmospheric Administration (NOAA) Hybrid Single Particle

237   Lagrangian Integrated Trajectory (HYSPLIT) trajectory model was used to identify source regions

238   of air masses at the three sites. The model runs were performed over twenty-four hours using the

239 NOAA NAM (Eta) Data Assimilation System (EDAS) data with a 40km×40km horizontal

240 resolution as input. Backward trajectories and trajectory clusters were calculated.

2.4 Model Evaluation

242 To evaluate the box model performance with observations, the following statistical

243 performance measures (Chang and Hanna, 2004; Hanna, 1988; Hanna et al., 1991, 1993), which

244 include the fractional bias (FB), the normalized mean square error (NMSE), the root mean square

245 error (RMSE), and the partition of NMSE due to systematic errors (NMSE$_s$) were used:

$$FB = \left(\overline{C_0} - \overline{C_p}\right)/0.5\left(\overline{C_0} + \overline{C_p}\right), \tag{5}$$

$$NMSE = \overline{\left(C_0 - C_p\right)^2}/\overline{C_0 C_p}, \tag{6}$$

$$RMSE = \sqrt{\overline{\left(C_0 - C_p\right)^2}}, \tag{7}$$

$$NMSE_s = 4FB^2/\left(4 - FB^2\right), \tag{8}$$

250 where C_p is model predictions, C_0 is observations, overbar $(\bar{C})$ is average over the dataset.

3 Results and Discussion

3.1 General characteristics in measured GOM and GEM

253 In the selected 83 cases, atmospheric GOM and GEM mixing ratios varied greatly at the

254 three sites (Fig. 2). Mixing ratios of GOM varied over 0.03–87.79 ppqv at AI, 0.04–4.93 ppqv at

255 TF, and 0–0.65 ppqv at PM. At AI and TF, significant diurnal variation was observed with

256 afternoon maximums and nighttime minimums. At AI, GOM peaked at 10 ppqv over 14:00–16:00

257 EDT and was ~ 5 ppqv at night, well above the LOD (~ 0.1 ppqv, from Sigler et al., 2009, the

258 same LOD for the instruments at the three sites). At TF, GOM mixing ratios peaked at 0.75 ppqv

259 at 17:00 EDT and were below LOD at night, before 08:00 EDT. The GOM diurnal cycle at PM

260 was different from that at AI and TF. At PM, averaged GOM had higher mixing ratios at night and

261 in the early morning than in the afternoon. However, the median values showed afternoon peaks

262 and nighttime minimums. The difference between average and median GOM diurnal cycles was

263 driven by 3 cases that had abnormally high GOM mixing ratios (> 0.6 ppqv) at night or in the early

264 morning relative to the average GOM mixing ratio through the day (~ 0.1 ppqv).

265 Mixing ratios of GEM ranged over 65–231 ppqv at AI, 60–213 ppqv at TF, and 121– 231

266 ppqv at PM (Fig. 2). On average, GEM mixing ratios at PM were 8% higher than that at TF and

267 12% higher than that at AI. Unlike GOM, GEM diurnal cycles showed nearly flat patterns at AI

268 and PM, though slightly higher (~ 3 %) GEM mixing ratios at night than in the daytime were

269 observed at PM. In contrast, the average GEM diurnal cycle at TF showed an early morning (07:00

270 EDT) minimum (112 ppqv) and a daytime (13:00 EDT) maximum (153 ppqv).

271 The site differences of GOM and GEM diurnal cycles could be attributed to different

272 chemical environments, land surface types, and meteorological conditions. For example, the GEM

273 daily minimum at night and in the early morning at TF was likely caused by a strong net loss

274 dominated by dry deposition under nocturnal inversion (Mao et al., 2008; Mao and Talbot, 2012).

275 Nocturnal inversion also influenced the GEM and GOM diurnal cycles at PM, albeit differently

276 from at TF. The elevation of PM site is 700ma.s.l., above the nocturnal inversion layer (< 200 m)

277 (e.g. Kutsher et al., 2012), and thus GEM and GOM at night were continuously replenished by

278 those produced from daytime and remaining in the residual layer, which likely caused higher

279 nighttime values at PM. Daytime peaks of GOM at TF and AI were most likely caused by

280 photochemical oxidation of GEM under strong solar radiation. The causes for such variation were

281 examined in Sect. 3.4.2.

282 **3.2 Simulated diurnal variation and speciation of GOM**

283   Model simulated diurnal cycles of GOM averaged over the 50, 12, and 21 clear-sky days

284 at AI, TF, and PM, respectively, were shown in Fig. 2. The patterns of diurnal variation were

285 similar at the three sites with small discrepancy on the occurring time of daily peaks (~ 13:00 LT

286 at AI, and ~14:00 LT at TF and PM), but the magnitude varied large by site. AI had the largest

287 GOM diurnal amplitude (i.e., daily maximum – daily minimum) ranging from 0.73 to 13.29 ppqv,

288 TF from 0.05 to 0.57 ppqv, and PM showed a very small range from 0.05 to 0.14 ppqv. Similar

289 magnitude variation was also exhibited in GOM observations (Fig. 2). Overall, simulated GOM

290 mixing ratios at the three sites were in agreement with observations (detailed comparison in Sect.

291 3.3).

292   The simulations suggested that the dominant GOM species and GEM oxidants varied by

293 site (Fig. 3). At AI, brominated GOM species comprised 59–81% of the total GOM over 08:00–

294 18:00 EDT, whereas HgO was dominant (50–92% of the total GOM) during the remaining day.

295 At TF and PM, HgO was the predominant GOM species (62–88%). HgO was produced from

296 oxidation of GEM by O_3 and OH. The contribution to HgO from oxidation by O_3 was larger than

297 by OH except at noon when OH mixing ratios reach daily peaks resulting in comparable

298 contributions (48 and 52% by OH and O_3, respectively). At AI, $BrHgNO_2$ and HgBrO were the

299 most abundant brominated GOM species, which constituted ~ 96% of the total brominated GOM.

300 HgBrO was produced from the GEM + BrO reaction, while $BrHgNO_2$ were produced from GEM

301 oxidation by Br radicals followed by reactions of HgBr with NO_2. $Hg(OH)_2$ from GEM oxidation

302 by H_2O_2 appeared to be an important nighttime GOM species at the inland site (PM), accounting

303 for 33% of the total GOM at night. Other GOM species were negligible in the studied cases.

304 **3.3 Model evaluation**

305   For all cases at AI and TF, the average simulated and observed GOM diurnal cycles agreed

306 reasonably well in both magnitude and shape, whereas at PM the model appeared to have missed

307 both (Fig. 2). Three salient features were noted for the disagreement between the model and

308 observational results. First, the standard deviation of observed GOM mixing ratios was a factor of

309 2–7 larger than that of the simulated. This suggested that the model could capture the mean values

310 of GOM, but not the very low and very large mixing ratios. Second, observed nighttime GOM

311 mixing ratios were 12–200% larger than the simulated at AI, indicating that the model did not

312 capture certain nighttime processes producing GOM in the MBL. Third, the simulated diurnal

313 cycle was the opposite of the observed at PM, with the maximum during the day and minimum at

314 night. It was likely that the model simply simulated the dependence of GOM production on solar

315 radiation. At PM, more processes may have contributed to the diurnal variation. At night, the site

316 is above the nocturnal boundary layer and exposed to the GOM produced in the preceding

317 convective boundary layer, which could continually replenish surface GOM at the site that was

318 lost via dry deposition and perhaps reduction. The model-observation discrepancies of GOM at

319 the three sites were discussed as follows.

320 3.3.1 Appledore Island (marine)

321   Of the 50 cases at AI, 27 diurnal cycles of GOM were simulated with the average values

322 and patterns close to the observed and $NMSE_s = 1.88\%$, denoted as *matching* cases hereafter, 8

323 were underestimated with $NMSE_s = 121\%$, and 15 were overestimated with $NMSE_s = 171\%$. The

324 observed and simulated average GOM mixing ratios and the corresponding ranges were calculated

325 for the matching, under-estimation, and over-estimation cases at AI (Fig. 4a). For more than half

326 of the time (27 matching cases out of 50 cases in total), the model captured the average GOM

327 diurnal cycle, the diurnal cycle pattern and overall GOM levels. Beyond that, Fig. 4a shows large

328 difference in the observed GOM levels among the matching, under-estimation, and over-

329 estimation cases. On average, the observed daytime peak in the under-estimation cases was about

330 twice as large as that for the matching cases and 7 times larger than that for the over-estimation

331 cases. However, such difference was not captured by the model, suggesting that some GOM

332 producing processes in the MBL were not included or not realistically represented in the box model.

333 In addition, the GOM diurnal pattern in the over-estimation cases was different from those in the

334 under-estimation and matching cases. The average observed GOM diurnal cycles of the under-

335 estimation and matching cases both exhibited a daily maximum at 13:00 EDT and a minimum over

336 04:00–08:00 EDT, whereas the over-estimation cases showed a daily maximum at around 20:00

337 EDT and a minimum at 07:00–08:00EDT.

338   Such differences were due possibly to the challenges of simulating Br and BrO in the MBL

339 at AI. No measurements of Br and BrO radicals as well as Br_2 were available at AI. To reasonably

340 simulate mixing ratios of Br and BrO, Br_2 mixing ratios were calculated based on the BrO

341 observations at a mid-latitude MBL site from Saiz-Lopez et al. (2006), which was ~5.6 ppqv during

342 the daytime (06:00–21:00 EDT). Saiz-Lopez et al. (2006) showed that daytime peak mixing ratios

343 of BrO in the MBL could vary by a factor of 2 over a time period of 3 days. Such variation was

344 not captured in our box model, potentially resulting in uncertainty of up to 100% in simulated Br

345 mixing ratios with subsequent effects on GOM simulation.

346   In the over-estimation cases, the simulated GOM daytime peaks were very low and

347 appeared later during the day than in the under-estimation and matching cases. Considering the

348 late afternoon peak (17:00 EDT) of O_3 compared to the noontime peak of Br radicals, O_3 possibly

349 played a more important role in the over-estimation cases. To verify this hypothesis, a sensitivity

350 simulation was conducted without the initial Br_2 mixing ratio fixed for these cases, termed as the

351 O_3/OH scenario. In this sensitivity runs, the Br_2 concentration rapidly diminished with time leading

352 to very low concentrations of Br and BrO. The O_3/OH scenario turned out to better represent these

353 15 overestimation cases with $NMSE_s = 34\%$ (compared to 167% with Br_2 mixing ratio fixed).

354 These sensitivity simulations suggested that in the MBL, Br may be a dominant GEM

355 oxidation most of the time, but at times of low Br mixing ratios, O_3 could become dominant. To

356 identify the origin of the air masses at AI, backward trajectory analysis was conducted using the

357 HYSPLIT4 model (https://ready.arl.noaa.gov/HYSPLIT.php). All 24 h backward trajectories

358 started from the time of GOM daily peaks for the 50 cases. The trajectory results were clustered

359 for over-estimation, matching, and under-estimation cases (Fig. 5). Based on these trajectories, in

360 about half of the 15 over-estimation cases air masses originated from marine environments, while

361 in more than 80% of the 27 matching cases and 7 out of 8 under-estimation cases air masses came

362 from inland northwest of AI. Note that in those under-estimation cases GOM mixing ratios were

363 exceptionally large, exceeding 30 ppqv.

364 Different source areas of air masses reaching AI could be one of the reasons for the large

365 variation of GOM observations. The highest levels of GOM were observed in summer with RH

366 roughly < 50% at AI (Mao et al., 2012). A close examination of the 50 cases at AI revealed low

367 RH levels ($\leq 45\%$) on 16 days. The time periods with RH $\leq 45\%$ appeared mostly (78% of the

368 time) in the afternoon over 12:00–20:00 EDT and less so (22%) at night over 21:00–02:00 EDT.

369 During these time periods, increased GOM (15 out of 16, compared with periods with high RH on

370 the same day) and daily maximum GOM (10 out of 16) occurred simultaneously at low RH,

371 regardless of the time of the day.

372 Interestingly, the RH level of 45% corresponds to the crystallization point of NaCl (Cziczo

373   et al., 1997; Tang et al., 1997). The crystallization of sea-salt aerosols might be link to the very

374   high GOM peaks in certain ways. Rutter and Schauer (2007) found that particles of potassium and

375   sodium chlorides had high partitioning coefficients that could shift the GOM gas-particle

376   partitioning toward the aqueous phase, while ammonium sulfate, levoglucosan, and adipic acid

377   would shift the partitioning toward the gas phase. It was thus *hypothesized* that, when these inland

378   air masses reached the MBL mixed with the marine air, the processes discussed above might have

379   been activated involving the interaction between land and marine air, which potentially resulted in

380   those very high GOM mixing ratios.

381   Laskin et al. (2012) found effective reactivity of chloride (Cl^-) components with organic

382   acid in sea salt aerosols (SSAs), possibly leading to depletion of Cl^- and formation of organic salts

383   in aerosols. Biogenic compounds in air masses originating from inland forested areas could be

384   oxidized forming organic acids in transit. As inland air reached the MBL, these organic acids

385   would deposit onto SSAs and could subsequently change SSAs' chemical and physical properties,

386   such as lowering concentrations of Cl^- and forming a thick organic film on the outside of SSAs.

387   The lower concentrations of Cl^- and higher concentrations of organic acid in aerosols might have

388   contributed to the shift in the gas-to-particle partitioning to the gas phase and resulted in higher

389   GOM mixing ratios in the atmosphere.

390   Another possible explanation could be air masses of inland origin encountering marine air

391   rich in atmospheric Br and BrO radicals. The main source of atmospheric Br is thought to come

392   from the release of Br_2 and BrCl from SSA (Finlayson-Pitts, 2010; Sander et al., 2003).

393   Experimental studies suggested Br^- enhancements of a factor of 40 to 140 on the surface of

394   sufficiently dry artificial SSA (Ghosal et al., 2008; Hess et al., 2007). Therefore, when drier inland

395   air masses were mixed with marine air in the MBL under relatively low RH conditions, SSA

396   became drier, forcing more Br_2 to be released from SSA, resulting in enhanced oxidation of GEM

397   by Br and BrO radicals. These hypotheses need to be validated in future research. These

398   mechanisms are presently missing in the box model, leading to the model's inability to capture

399   very high GOM mixing ratios. Measurements of halogen species and a better gas-particle

400   partitioning mechanism are needed to better the model's performance.

401   3.3.2   Thompson Farm (coastal)

402   Generally, the box model performed well at TF (Fig. 2) with overall $NMSE_s$ = 0.75% and

403   RMSE= 0.78 ppqv. Of the 12 cases at TF, 6diurnal cycles of GOM (50%) were simulated

404   reasonably well with $NMSE_s$ < 50%, 2 were underestimated by ~ 70%, and 4 cases were

405   overestimated by a factor of 2to 5. Overall, the observed average diurnal cycles of GOM for all

406   selected summer clear-sky days at TF had daily peaks during 14:00–20:00 EDT with very low

407   values at night between 0:00 and 8:00 EDT (Sigler et al., 2009) (Fig. 2). The peak observed at

408   17:00 EDT (Fig. 2) was largely affected by the abnormally high GOM peak in that one under-

409   estimation case (Fig. 4b).

410   For the over-estimation and matching cases, the model reproduced very low GOM mixing

411   ratios at night (Fig. 4b). For the same reason substantially lowering GOM mixing ratios at night

412   and in the early morning at TF (Mao et al., 2008), the low nighttime GOM at TF was probably

413   caused by loss via dry deposition under nocturnal inversion. To capture these low values in model

414   simulations, realistic nocturnal boundary layer height data were needed beside solid representation

415   of dry deposition and chemistry in the model. The diurnal cycle of boundary layer height in the

416   box model was parameterized based on reanalysis data obtained from the Research Data Archive

417   at the National Center for Atmospheric Research (http://rda.ucar.edu/datasets/ds093.0/). Use of

418   these data helped to reproduce the low nighttime GOM levels in simulations for the TF site.

419   Another notable feature in Fig. 4b is the exceedingly high observed GOM mixing ratios in the

420   under-estimation cases and the low observed GOM mixing ratios throughout the day in all over-

421   estimation cases. Observed GOM mixing ratios in the under-estimation cases showed a factor of

422   3–4 larger than those in the matching cases, and a factor of 3–31 larger than those in the over-

423   estimation cases (Fig. 4b). Concurrently, larger fine particle concentrations, 7468 cm^{-3} on average,

424   were observed for the under-estimation cases, which was 51 and 80% larger than those in the

425   matching cases and over-estimation cases, respectively. Lower RH, 66% on average, was observed

426   in the under-estimation cases, 5and 11% lower than that in the matching and over-estimation cases,

427   respectively. Moreover, higher air pressure (1018, 8 and 12 hPa larger than the matching and over-

428   estimation cases, respectively), lower wind speed (0.8 m s^{-1} on average, 35 and 68% lower than

429   matching and over-estimation cases respectively), and stronger solar radiation flux (8 and 13%

430   stronger than matching and over-estimation cases respectively) were found in the under-estimation

431   cases. An examination of the sea level pressure maps (Figure S1) in the under-estimation cases

432   suggested that these cases occurred under the strongest Bermuda High influence, with the calmest,

433   sunniest, and driest conditions of all cases, which is most conducive to photochemistry and

434   pollution build-up that may have ultimately contributed to the very large GOM mixing ratios in

435   those under-estimation cases. Our model appeared to fail to mimic the chemistry under such

436   conditions that produced the largest GOM mixing ratios.

437   3.3.3   Pack Monadnock (inland, rural, elevated site)

438   At PM, diurnal cycles of GOM were overestimated with $NMSE_s$ = 70% and overall

439   RMSE= 0.13 ppqv. However, considering the extremely low mixing ratios of GOM observed at

440   PM (Fig. 2), cases with RMSE < 0.1 ppqv (LOD) were considered as matching cases. Therefore,

441   the model reasonably simulated 11 out of 21 (52%) cases, underestimated in 1, and overestimated

442   in 9. Evaluation of simulated GOM diurnal cycles against observations (Fig. 2) showed reasonable

443   agreement with general overestimation ranging over 0.05–0.07 ppqv.

444   The observed GOM diurnal cycle (Fig. 2f) showed daily maximums at 08:00 and 23:00

445   EDT, which were mainly influenced by the underestimated case (Fig. 4c). In comparison, the

446   remaining (95 %) cases showed a very flat GOM diurnal cycle at PM. The first and most important

447   reason for such observation-model discrepancy is that the PM site is a mountain site (700 m a.s.l.),

448   which is above the nocturnal inversion layer (~200m at TF) but within the convective boundary

449   layer during the day. At night, a regional pool of GOM produced in the preceding convective

450   boundary layer remained in the residual layer, which kept the surface GOM levels from dropping

451   below the LOD at night at PM. The slight decline of GOM mixing ratios after sunrise was because

452   of mixing with the lower altitude air masses with depleted GOM from the night. The effect of the

453   PM's site characteristics was not represented in the box model, which could result in model's

454   inability to simulate diurnal variation associated with this aspect of the site. In addition, due to the

455   dominance of GEM oxidation by O_3 in GOM production in the model, it was highly likely that the

456   flat diurnal cycles (slightly higher at night) of GEM (Fig. 2) and O_3 were mirrored in GOM mixing

457   ratios.

458

459   **3.4   Sensitivity analysis**

460   3.4.1   Sensitivity of GOM to physical and chemical parameters

461   The base scenario (*Scenario* 0) of these sensitivity runs represented the real atmospheric

462   conditions on the selected 50 days at AI. *Scenarios* 1–10 are sensitivity runs where one parameter

463   in the base scenario was changed at the time (Table 3). *Scenario* 1 turned off photolysis reactions.

464   *Scenarios* 2–4 tested the gas-particle partitioning scheme. The liquid water content range was

465 derived from Hedgecock et al. (2003). *Scenarios* 5–9tested the sensitivity of GOM mixing ratios

466 to GEM oxidation reactions and their coefficients. *Scenarios* 10–11 tested the sensitivity of GOM

467 mixing ratios to temperature. The temperature range was based on the observed average

468 temperature diurnal cycle.

469   The importance of photochemical radicals in GEM oxidation was demonstrated clearly in

470 decreases of 3-92 and 2-100 % in daytime GOM and PBM, respectively with largest decreases at

471 noon as a result of turning off photochemistry (*Scenario 1*). *Scenario 2* showed ~74% of oxidized

472 Hg transformed to PBM at AI with gas-particle partitioning switched on. In this scenario, HgO

473 and $Hg(OH)_2$ were more sensitive than halogenated GOM species (such as $BrHgNO_2$). Turning

474 off gas-particle partitioning more than quadrupled the mixing ratios of HgO and $Hg(OH)_2$

475 throughout the day compared to increases of more than 100 and 60% halogenated GOM species

476 during daytime and nighttime, respectively.

477   Decreasing liquid water content by 1 order of magnitude tripled GOM mixing ratios,

478 whereas increasing the same amount decreased GOM by 80% (*Scenarios 3–4*). Sensitivity of

479 GOM and PBM mixing ratios to dominant GEM oxidation reactions are shown in *Scenarios 5–9*.

480 Using the slowest rate coefficient of GEM + O_3 obtained from Hall (1995), as opposed to the one

481 from Snider et al. (2008) led to a decrease of 56.7% in HgO, and decreases of 15 and 85% in total

482 GOM during daytime and nighttime, respectively. Using an order of magnitude faster rate

483 coefficient of GEM + Br from Ariya et al. (2002) increased 250% of total GOM during daytime.

484 Turning off GEM oxidation by O_3, OH, or Br resulted in decreases of 16, 10, and 48%, respectively,

485 in daytime GOM mixing ratios. Turning off the GEM + Br oxidation reaction also decreased

486 daytime PBM mixing ratios by 60%. However, for nighttime GOM and PBM mixing ratios,

487 turning off the GEM + O_3 reaction caused decreases of 88 and 51%, respectively, since Br and OH

488 are both photochemical radicals and O_3 was the predominant oxidant for GEM in the model.

489 *Scenarios 10–11* suggested that nighttime GOM and PBM mixing ratios were more

490 sensitive to temperature than those during daytime. Increasing temperature by 10 K caused a 9%

491 increase each in GOM and PBM mixing ratios during daytime but a decrease of 13% in GOM and

492 54% in PBM at night. This was because the rate coefficient of GEM + O_3 increases with increasing

493 temperature, but the rate coefficient of GEM + OH decreases with increasing temperature.

494 In summary, the parameters used in gas-particle partitioning process, including solar

495 radiation values, temperature, and the rate coefficients of major GEM oxidation reaction, could all

496 affect the GOM simulation but with varying degree. Aerosol properties were suggested to play a

497 very important role in the partitioning of ambient GOM and PBM species and thus should be better

498 represented in future Hg model simulation studies. Using a slower rate coefficient of GEM + O_3

499 (Hall, 1995) had similar effects as not including the GEM + O_3 reaction, i.e. decreasing GOM

500 mixing ratios, especially at nighttime, and brominated GOM species becoming dominant. The

501 GEM + OH reaction was not as important as GEM + O_3 or Br. The use of a higher GEM + Br rate

502 coefficient derived from the study by Ariya et al. (2002) caused more than a factor of 3 higher

503 GOM and PBM resulting in overestimated GOM for most cases. GOM and PBM production

504 appeared to favor lower temperature at daytime and higher temperature at night, and simulated

505 GOM concentrations were not as sensitive to temperature change as to solar radiation and gas-

506 particle partitioning.

507 3.4.2   Influence of physical and chemical processes on GOM diurnal cycle

508 Large variations were exhibited in both observed and simulated GOM mixing ratios at AI,

509 TF, and PM (Fig. 2). Considering that all cases were under relatively calm, clear-sky conditions,

510   the simulated GOM mixing ratio and diurnal cycle were controlled primarily by chemical reactions,

511   dry deposition, and gas-particle partitioning. To quantify the contribution of processes to the

512   difference of GOM mixing ratios at the three sites, two sensitivity scenarios were conducted: use

513   the same physical parameters as those of AI for TF (denoted as TF_AIaerodry) and PM (denoted

514   as PM_AIaerodry).

515   Comparison of simulated GOM diurnal cycles from the AI, TF_AIaerodry and

516   PM_AIaerodry scenarios showed the influence of different chemical scenarios on GOM mixing

517   ratios at the three sites. At night, GOM mixing ratios at the three sites did not vary significantly

518   (0-2 ppqv), with higher values at PM than those at AI and TF (Fig. 6). However, the mid-day peak

519   at AI was more than a factor of two greater than those in the PM_AIaerodry and TF_AIaerodry

520   scenarios, indicating more chemical transformation of Hg occurring at AI. The daytime mixing

521   ratios of GOM at TF and PM were similar, while the nighttime GOM mixing ratios at PM were

522   30-52% higher than at AI and 20-200% higher than at TF. This probably resulted from larger

523   nighttime GEM and O_3 mixing ratios, hence producing more GOM, at PM than at TF and AI.

524   Specifically, nighttime GEM mixing ratios at PM were 8-15% higher than at AI and 8-34% higher

525   than TF cases, while nighttime O_3 mixing ratios at PM were 11-70% larger than at AI and 35-260%

526   larger than at TF. PM had higher nighttime GEM and O_3 mixing ratios, because this site was

527   exposed in the residual boundary layer at night due to its high elevation, constantly replenished

528   with the regional pool of air from the preceding convective boundary layer. Overall, chemical

529   transformation contributed ~60% of the daytime difference in GOM between AI and the two sites

530   over land (TF and PM), 33% of the nighttime difference between AI and TF, and 26% of the

531   difference between PM and AI.

532   In summary, the sensitivity scenarios suggested that dry deposition and gas-particle

533   partitioning contributed 4-37% and 30-96%, respectively, of the total GOM difference between AI

534   and PM. Both processes had larger contributions at night that during daytime. Dry deposition

535   contributed 6-24% of the GOM difference between AI and TF and gas-particle partitioning 18-

536   78%.

537   3.4.3   Br chemistry in the MBL

538   Diurnal cycles of Br and BrO radicals (Fig. 7) were simulated using the Br chemical

539   mechanism described in Sect. 2. Photodissociation of Br_2 was the main source of Br and BrO

540   radicals during daytime. Our simulations suggested that reactive Br compounds were significant

541   gaseous oxidants of GEM in the MBL at a fixed initial mixing ratio of 5.6 ppqv for Br_2. Increasing

542   initial mixing ratios of Br_2 by 25% resulted in an increase of 0.01–2.15 ppqv in GOM mixing ratios.

543   In addition, the reaction of BrO with methyldioxy (CH_3O_2) radicals could have important

544   influence on the mixing ratios of Br, BrO, and GOM. Simulated daytime mixing ratios of CH_3O_2

545   was ~ 40 pptv, and the rate coefficient of $(5.7\pm0.6) \times 10^{-12}$ cm^3 $molecule^{-1}$ s^{-1} at 298 K for BrO +

546   CH_3O_2 (Aranda et al., 1997) was used for our simulations. Pathways B1, B2, and B3 were

547   suggested by Aranda et al. (1997) based on an experimental study (Table 4). However, the

548   production of CH_3O may be due to its self-reaction in B1. Guha and Francisco (2003) suggested

549   CH_3OOOBr to be a likely intermediate of this reaction, and that CH_3OOOBr could dissociate to

550    $CH_2O+HOOBr$ (B4, Table 4). Based on thermodynamics calculations, CH_3OBr and O_2 (B3, Table

551   4) were possible products. BrOO and HOBr were both included in the Br chemical cycle and can

552   be transformed back to Br and BrO radicals in the model. However, it is unclear whether CH_3OBr

553   (product of B3) or HOOBr (product of B4) could be transformed back to Br and BrO radicals in

554 the atmosphere. In this case, using the B3 or B4 pathway did not appear to make a difference in

555 our box model results.

556   In this study, the B1 and B2 pathways were used for the CH_3O_2 +BrO reaction as part of

557 the base scenario (denoted as Sim-avg BrOO). The sensitivity run Sim-avg CH_3OBr used the B3

558 pathway in lieu of B1 and B2. The simulated average and the range of GOM diurnal cycles in the

559 base and sensitivity scenarios were evaluated against observed mean and median GOM diurnal

560 cycles of the 50 study cases at AI (Fig. 8). If the CH_3O_2 +BrO reaction followed the B1 and B2

561 pathways, this reaction had a negligible effect on reactive Br radicals. However, if B3 or B4 was

562 applied, the simulated total GOM mixing ratio was lowered by 50% during daytime. Moreover,

563 the simulated GOM diurnal cycle in the base scenario agreed favorably with the observed average

564 GOM diurnal cycle (NMSE= 15 %), while the results of the Sim-avg CH_3OBr scenario were in

565 better agreement with the observed median GOM diurnal cycle (NMSE= 14%). These agreements

566 indicated that, if the BrO+CH_3O_2 reaction was a net sink of BrO radicals, the model was able to

567 simulate most cases better, whereas if the product of BrO+CH_3O_2 was transformed back to Br or

568 BrO radicals, the model appeared to capture those cases with large GOM mixing ratios (> 6 ppqv).

569 Due to the scarcity of kinetic research on the B3 and B4 pathways, we used B1 and B2 pathways

570 for CH_3O_2 +BrO reaction in this study.

571   In short, the pathways of BrO+CH_3O_2 could play an important role in atmospheric Br

572 chemistry and Hg speciation in Br-rich environments. Research on the reaction pathways and rate

573 coefficients of the BrO+CH_3O_2 reaction is warranted to better assess the role of this reaction.

574 **4   Summary**

575   This study provided a state-of-the-art chemical mechanism with most up-to-date Hg and

576 halogen chemistry and tested the mechanism for three different environments using a mercury box

577   model. Eighty-three summer clear-sky days were selected at marine, coastal, and inland elevated

578   sites in southern New Hampshire to evaluate the model. As a result, for each of the three

579   environments, GOM diurnal cycles of over half selected cases were reasonably represented by the

580   box model. It was hypothesized, based on the key results and discussion presented in Section 3,

581   that dry air masses with organic compounds transported from inland may result in very large GOM

582   mixing ratios in the MBL possibly due to changing physical and chemical properties of sea salt

583   aerosols. The low nighttime and morning GOM mixing ratios at coastal site were likely a result of

584   a net loss due to dry deposition in the nocturnal inversion layer. The GOM mixing ratios above the

585   LOD at the inland site at night were probably caused by constant replenishment from a regional

586   pool, in the residual boundary layer, of GOM that was produced in the preceding daytime

587   convective boundary layer. The updated chemical mechanism largely improved the simulation of

588   the magnitude and pattern of GOM diurnal variation at the coastal and inland sites. HgO produced

589   from oxidation of GEM by O_3 and OH dominated GOM species at the coastal and inland sites,

590   while bromine-induced mercury species (mainly BrHgOOH, BrHgOBr, and HgBrO) were

591   important at the marine site. In Br chemistry, the products of the CH_3O_2 +BrO reaction strongly

592   influenced the simulated Br and Hg concentrations. In this study, GEM oxidation by O_3 and OH

593   was represented in ways similar to those in regional and global models, which is limited by the

594   current nebulous understanding of potential surface chemistry.

595   It should be noted that without measurements of speciated GOM, modeling results cannot

596   be used to conclusively identify the dominant oxidants of Hg, as well as dominant GOM species

597   in that matter, in the atmosphere. Indeed, the potential uncertainty in ambient Hg measurements

598   especially GOM is a major concern in the community. That being said, it is unlikely to have a

599   quantitative understanding of the bias of our GOM concentrations. Recent laboratory experiments

600   and reviews (Lyman et al., 2010; Jaffe et al., 2014; McClure et al., 2014; Huang and Gustin, 2015;

601   Gustin et al., 2015) reported O_3 and relative humidity (RH) interferences on mercury halides for

602   KCl-coated denuder, the part of Tekran 1130 unit commonly used for GOM field measurements.

603   As stated in Section 2, in our GOM measurement the RH effect was minimized by adding

604   refrigeration to remove excess of water in the airsteam. O_3 interference and bias low GOM

605   collection efficiency of KCl-coated denuders were limited to a handful of GOM species in

606   laboratory experiments and remain untested in field measurements. If the measured GOM

607   concentrations were indeed biased low by a factor of 2 or 3 under certain conditions as previous

608   studies speculated, the matching cases at AI and TF would be reduced from 50% of the total cases

609   to 30%, and the model would potentially underestimate GOM concentrations in the remaining

610   cases (70%) by a factor of 3 to 4. It is however hard to speculate the effect at PM since most GOM

611   observations there were below the LOD. This suggested even greater unknowns in our

612   understanding of Hg chemistry. Therefore, more experimental or theoretical studies on Hg

613   reactions and better GOM measurement data are warranted to improve our understanding and

614   subsequently model simulations of atmospheric Hg cycling, which can ultimately serve policy-

615   making in an effective manner.

Acknowledgements

617   This work is funded by NSF AGS grant # 1141713. We thank T. Dibble, Y. Zhou, Y. Zhang, and

618   C. B. Hall for valuable suggestions and help. We are grateful to the three anonymous reviewers

619   for their thoughtful, detailed, constructive comments, which helped to improve the clarity of the

620   paper.

621

References

Aranda, A., Le Bras, G., La Verdet, G., and Poulet, G.: The BrO + CH_3O_2 reaction: kinetics and role in the atmospheric ozone budget, Geophys. Res. Lett., 24, 2745–2748, 1997.

Ariya, P. A., Khalizov, A., and Gidas, A.: Reactions of gaseous mercury with atomic and molecular halogens: kinetics, product studies, and atmospheric implications, J. Phys. Chem. A, 106, 7310–7320, 2002.

Ariya, P. A., Amyot, M., Dastoor, A., Deeds, D., Feinberg, A., Kos, G., Poulain, A., Ryjkov, A., Semeniuk, K., Subir, M., and Toyota, K.: Mercury physicochemical and biogeochemical transformation in the atmosphere and at atmospheric interfaces: a review and future directions, Chem. Rev., 115, 3760–3802, doi:10.1021/cr500667e, 2015.

Atkinson, R., Baulch, D. L., Cox, R. A., Crowley, J. N., Hampson, R. F., Hynes, R. G., Jenkin, M. E., Rossi, M. J., and Troe, J.: Evaluated kinetic and photochemical data for atmospheric chemistry: Volume I – gas phase reactions of Ox, HOx, NOx and SOx species, Atmos. Chem. Phys., 4, 1461–1738, doi:10.5194/acp-4-1461-2004, 2004.

Atkinson, R., Baulch, D. L., Cox, R. A., Crowley, J. N., Hampson, R. F., Hynes, R. G., Jenkin, M. E., Rossi, M. J., Troe, J., and Wallington, T. J.: Evaluated kinetic and photochemical data for atmospheric chemistry: Volume IV – gas phase reactions of organic halogen species, Atmos. Chem. Phys., 8, 4141–4496, doi:10.5194/acp-8-4141-2008, 2008.

Balabanov, N. B., Shepler, B. C., and Peterson, K. A.: Accurate global potential energy surface and reaction dynamics for the ground state of $HgBr_2$, J. Phys. Chem. A, 109, 8765–8773, 2005.

Baumgardner, D., Raga, G. B., Kok, G., Ogren, J., Rosas, I., Báez, A., and Novakov, T.: On the evolution of aerosol properties at a mountain site above Mexico City, J. Geophys. Res. -Atmos., 105, 22243–22253, doi: 10.1029/2000JD900299, 2000.

Bergan, T. and Rodhe, H.: Oxidation of elemental mercury in the atmosphere; constraints imposed by global scale modelling, J. Atmos. Chem., 40, 191–212, 2001.

Bergan, T., Gallardo, L., and Rodhe, H.: Mercury in the global troposphere: a three-dimensional model study, Atmos. Environ., 33, 1575–1585, 1999.

Chang, J. C. and Hanna, S. R.: Air quality model performance evaluation, Meteorol. Atmos. Phys., 87, 167–196, doi: 10.1007/s00703-003-0070-7, 2004.

Clarkson, T. W.: The toxicity of mercury and its compounds, in: Mercury Pollution: Integration and Synthesis, edited by: Watras, C. J. and Huckabee, J.W., Boca Raton, FL, USA, 631–641, 1994.

Cziczo, D. J., Nowak, J. B., Hu, J. H., and Abbatt, J. P. D.: Infrared spectroscopy of model tropospheric aerosols as a function of relative humidity: observation of deliquescence and crystallization, J. Geophys. Res.-Atmos., 102, 18843–18850, 1997.

Dibble, T. S., Zelie, M. J., and Mao, H.: Thermodynamics of reactions of ClHg and BrHg radicals with atmospherically abundant free radicals, Atmos. Chem. Phys., 12, 10271–10279, doi:10.5194/acp-12-10271-2012, 2012.

Donohoue, D. L., Bauer, D., and Hynes, A. J.: Temperature and pressure dependent rate coefficients for the reaction of Hg with Cl and the reaction of Cl with Cl: a pulsed laser photolysispulsed laser induced fluorescence Study, J. Phys. Chem. A, 109, 7732–7741, 2005.

Finlayson-Pitts, B. J.: Halogens in the troposphere, Anal. Chem., 82, 770–776, doi: 10.1021/ac901478p, 2010.

Finley, B. D. and Saltzman, E. S.: Observations of Cl_2, Br_2, and I_2 in coastal marine air, J. Geophys. Res., 113(D21), D21301, doi:10.1029/2008JD010269, 2008.

Fischer, E. V., Ziemba, L. D., Talbot, R.W., Dibb, J. E., Griffin, R. J., Husain, L., and Grant, A. N.: Aerosol major ion record at Mount Washington, J. Geophys. Res.-Atmos., 112, D02303, doi: 10.1029/2006JD007253, 2007.

Ghosal, S., Brown, M. A., Bluhm, H., Krisch, M. J., Salmeron, M., Jungwirth, P., and Hemminger, J. C.: Ion partitioning at the liquid/vapor interface of a multicomponent alkali halide solution: a model for aqueous sea salt aerosols, J. Phys. Chem. A, 112, 12378–12384, 2008.

Glasow, R. V., Sander, R., Bott, A., and Crutzen, P. J.: Modeling halogen chemistry in the marine boundary layer 1. Cloud-free MBL, J. Geophys. Res.-Atmos., 107, 9-1–9-16, 2002.

Goodsite, M. E., Plane, J. M. C., and Skov, H.: A theoretical study of the oxidation of HgO to $HgBr_2$ in the troposphere, Environ. Sci. Technol., 38, 1772–1776, 2004.

Goodsite, M. E., Plane, J. M. C., and Skov, H.: Erratum: A theoretical study of the oxidation of HgO to $HgBr_2$ in the troposphere, (Environ. Sci. Technol. (2004) 38:6 (1772–1776) doi: 10.1021/es034680s), Environ. Sci. Technol., 46, 5262, doi: 10.1021/es301201c, 2012.

Guha, S. and Francisco, J. S.: An ab initio study of the pathways for the reaction between CH_3O_2 and BrO radicals, J. Chem. Phys., 118, 1779–1793, doi:10.1063/1.1531099, 2003.

Gustin, M. S., Huang, J., Miller, M. B., Peterson, C., Jaffe, D. A., Ambrose, J., Finley, B. D., Lyman, S. N., Call, K., Talbot, R., Feddersen, D., Mao, H. and Lindberg, S. E.: Do we understand what the mercury speciation instruments are actually measuring? Results of RAMIX, Environmental Science and Technology, 47(13), 7295–7306, 2013.

Gustin, M. S., Amos, H. M., Huang, J., Miller, M. B., and Heidecorn, K.: Measuring and modeling mercury in the atmosphere: a critical review, Atmos. Chem. Phys., 15, 5697–5713, doi: 10.5194/acp-15-5697-2015, 2015.

Hall, B.: The gas phase oxidation of elemental mercury by ozone, Water Air Soil Poll., 80, 301–315, 1995.

690   Hanna, S. R.: Air quality model evaluation and uncertainty, JAPCA J. Air Waste Ma., 38, 406–
691   412, doi: 10.1080/08940630.1988.10466390, 1988.

692   Hanna, S. R., Strimaitis, D. G., and Chang, J. C.: Hazard response modeling uncertainty (a
693   quantitative method), vol. I: User's guide for software for evaluating hazardous gas dispersion
694   models; vol. II: Evaluation of commonly-used hazardous gas dispersion models; vol. III:
695   Components of uncertainty in hazardous gas dispersion models, Sigma Research Corporation,
696   Westford, USA, 1991.

697   Hanna, S. R., Chang, J. C., and Strimaitis, D. G.: Hazardous gas model evaluation with field
698   observations, Atmos. Environ. A-Gen., 27, 2265–2285, doi: 10.1016/0960-1686(93)90397-H,
699   1993.

700   Hedgecock, I. M. and Pirrone, N.: Chasing quicksilver: modeling the atmospheric lifetime of Hg^0
701   (g) in the marine boundary layer at various latitudes, Environ. Sci. Technol., 38, 69–76, 2004.

702   Hedgecock, I. M. and Pirrone, N.: Modelling chemical and physical processes of Hg compounds
703   in the marine boundary layer, Dyn. Mercury Pollut. Reg. Glob. Scales Atmospheric Process. Hum.
704   Expo. World, 2005.

705   Hedgecock, I. M., Pirrone, N., Sprovieri, F., and Pesenti, E.: Reactive gaseous mercury in the
706   marine boundary layer: modelling and experimental evidence of its formation in the Mediterranean
707   region, Atmos. Environ., 37, S41–S49, 2003.

708   Hess, M., Krieger, U. K., Marcolli, C., Huthwelker, T., Ammann, M., Lanford, W. A., and Peter,
709   T.: Bromine enrichment in the near-surface region of Br-doped NaCl single crystals diagnosed by
710   rutherford backscattering spectrometry, J. Phys. Chem. A, 111, 4312–4321, 2007.

711   Holmes, C. D., Jacob, D. J., and Yang, X.: Global lifetime of elemental mercury against oxidation
712   by atomic bromine in the free troposphere, Geophys. Res. Lett., 33, L20808, doi:
713   10.1029/2006GL027176, 2006.

714   Holmes, C. D., Jacob, D. J., Mason, R. P., and Jaffe, D. A.: Sources and deposition of reactive
715   gaseous mercury in the marine atmosphere, Atmos. Environ., 43, 2278–2285, 2009.

716   Holmes, C. D., Jacob, D. J., Corbitt, E. S., Mao, J., Yang, X., Talbot, R., and Slemr, F.: Global
717   atmospheric model for mercury including oxidation by bromine atoms, Atmos. Chem. Phys., 10,
718   12037–12057, doi:10.5194/acp-10-12037-2010, 2010.

719   Huang, J., Miller, M. B., Weiss-Penzias, P. and Gustin, M. S.: Comparison of gaseous oxidized
720   Hg measured by KCl-coated denuders, and nylon and cation exchange membranes, Environmental
721   Science and Technology, 47(13), 7307–7316, 2013.

722   Jaffe, D. A., Lyman, S., Amos, H. M., Gustin, M. S., Huang, J., Selin, N. E., Levin, L., ter Schure,
723   A., Mason, R. P., Talbot, R., Rutter, A., Finley, B., Jaeglé, L., Shah, V., McClure, C., Ambrose,
724   J., Gratz, L., Lindberg, S., Weiss-Penzias, P., Sheu, G.-R., Feddersen, D., Horvat, M., Dastoor, A.,
725   Hynes, A. J., Mao, H., Sonke, J. E., Slemr, F., Fisher, J. A., Ebinghaus, R., Zhang, Y., and Edwards,

726   G.: Progress on understanding atmospheric mercury hampered by uncertain measurements,
727   Environ. Sci. Technol., 48, 7204–7206, doi: 10.1021/es5026432, 2014.

728   Kim, P.-R., Han, Y.-J., Holsen, T. M., and Yi, S.-M.: Atmospheric particulate mercury:
729   concentrations and size distributions, Atmos. Environ., 61, 94–102, 2012.

730   Kim, S. Y., Talbot, R., Mao, H., Blake, D. R., Huey, G., and Weinheimer, A. J.: Chemical
731   transformations of Hg during Arctic mercury depletion events sampled from the NASA DC-8,
732   Atmos. Chem. Phys. Discuss., 10, 10077–10112, doi: 10.5194/acpd-10-10077-2010, 2010.

733   Kutsher, J., Haikin, N., Sharon, A., and Heifetz, E.: On the formation of an elevated nocturnal
734   inversion layer in the presence of a low-level jet: a case study, Bound.-Lay. Meteorol., 144, 441–
735   449, doi:10.1007/s10546-012-9720-y, 2012.

736   Laskin, A., Moffet, R. C., Gilles, M. K., Fast, J. D., Zaveri, R. A., Wang, B., Nigge, P., and
737   Shutthanandan, J.: Tropospheric chemistry of internally mixed sea salt and organic particles:
738   surprising reactivity of NaCl with weak organic acids, J. Geophys. Res.-Atmos., 117, D15302, doi:
739   10.1029/2012JD017743, 2012.

740   Laurier, F. and Mason, R.: Mercury concentration and speciation in the coastal and open ocean
741   boundary layer, J. Geophys. Res.-Atmos., 112, D06302, doi: 10.1029/2006JD007320, 2007.

742   Laurier, F. J. G., Mason, R. P., Whalin, L., and Kato, S.: Reactive gaseous mercury formation in
743   the North Pacific Ocean's marine boundary layer: a potential role of halogen chemistry, J. Geophys.
744   Res.-Atmos., 108, ACH3-1—ACH3-12, doi: 10.1029/2003JD003625, 2003.

745   Lewis, E. R. and Schwartz, S. E.: Comment on "Size distribution of sea-salt emissions as a function
746   of relative humidity," Atmos. Environ., 40, 588–590, doi: 10.1016/j.atmosenv.2005.08.043, 2006.

747   Lin, C.-J. and Pehkonen, S. O.: Aqueous phase reactions of mercury with free radicals and chlorine:
748   implications for atmospheric mercury chemistry, Chemosphere, 38, 1253–1263, 1999.

749   Lin, C.-J., Pongprueksa, P., Lindberg, S. E., Pehkonen, S. O., Byun, D., and Jang, C.: Scientific
750   uncertainties in atmospheric mercury models I: Model science evaluation, Atmos. Environ., 40,
751   2911–2928, 2006.

752   Lindberg, S. E., Brooks, S., Lin, C.-J., Scott, K. J., Landis, M. S., Stevens, R. K., Goodsite, M.,
753   and Richter, A.: Dynamic oxidation of gaseous mercury in the arctic troposphere at polar sunrise,
754   Environ. Sci. Technol., 36, 1245–1256, 2002.

755   Madronich, S.: UV radiation in the natural and perturbed atmosphere, in: Environmental Effects
756   of   UV,   CRC   Press,   Boca   Raton,   FL,   USA,   available   at:
757   http://opensky.library.ucar.edu/collections/OSGC-000-000-020-698 (last access: 16 April 2015),
758   1993.

759   Mao, H. and Talbot, R.: O_3 and CO in New England: temporal variations and relationships, J.
760   Geophys. Res.-Atmos., 109, D21304, doi: 10.1029/2004JD004913, 2004.

761 Mao, H., Talbot, R. W., Sigler, J. M., Sive, B. C., and Hegarty, J. D.: Seasonal and diurnal
762 variations of Hg over New England, Atmos. Chem. Phys., 8, 1403–1421, doi: 10.5194/acp-8-1403-
763 2008, 2008.

764 Mao, H., Talbot, R., Hegarty, J., and Koermer, J.: Speciated mercury at marine, coastal, and inland
765 sites in New England – Part 2: Relationships with atmospheric physical parameters, Atmos. Chem.
766 Phys., 12, 4181–4206, doi: 10.5194/acp-12-4181-2012, 2012.

767 Mason, R. P., Kim, E.-H., Cornwell, J., and Heyes, D.: An examination of the factors influencing
768 the flux of mercury, methylmercury and other constituents from estuarine sediment, Mar. Chem.,
769 102, 96–110, 2006.

770 Miller, C. L., Mason, R. P., Gilmour, C. C., and Heyes, A.: Influence of dissolved organic matter
771 on the complexation of mercury under sulfidic conditions, Environ. Toxicol. Chem., 26, 624–633,
772 2007.

773 Moldanová, J. and Ljungström, E.: Sea-salt aerosol chemistry in coastal areas: a model study, J.
774 Geophys. Res.-Atmos., 106, 1271–1296, doi: 10.1029/2000JD900462, 2001.

775 Obrist, D., Tas, E., Peleg, M., Matveev, V., Faïn, X., Asaf, D., and Luria, M.: Bromine-induced
776 oxidation of mercury in the mid-latitude atmosphere, Nat. Geosci., 4, 22–26, 2011.

777 Pal, B. and Ariya, P. A.: Gas-phase HO-initiated reactions of elemental mercury: kinetics, product
778 studies, and atmospheric implications, Environ. Sci. Technol., 38, 5555–5566, 2004a.

779 Pal, B. and Ariya, P. A.: Studies of ozone initiated reactions of gaseous mercury: kinetics, product
780 studies, and atmospheric implications, Phys. Chem. Chem. Phys., 6, 572–579, 2004b.

781 Pillai, P. S. and Moorthy, K. K.: Aerosol mass-size distributions at a tropical coastal environment:
782 response to mesoscale and synoptic processes, Atmos. Environ., 35, 4099–4112, doi:
783 10.1016/S1352-2310(01)00211-4, 2001.

784 Poissant, L., Pilote, M., Beauvais, C., Constant, P. and Zhang, H. H.: A year of continuous
785 measurements of three atmospheric mercury species (GEM, RGM and Hgp) in southern Québec,
786 Canada, Atmospheric Environment, 39(7), 1275–1287, 2005.

787 Raofie, F. and Ariya, P. A.: Product study of the gas-phase BrO-initiated oxidation of Hg^0:
788 Evidence for stable Hg^{1+} compounds, Environ. Sci. Technol., 38, 4319–4326, 2004.

789 Rolfhus, K. R., Sakamoto, H. E., Cleckner, L. B., Stoor, R. W., Babiarz, C. L., Back, R. C.,
790 Manolopoulos, H., and Hurley, J. P.: Distribution and fluxes of total and methylmercury in Lake
791 Superior, Environ. Sci. Technol., 37, 865–872, 2003.

792 Rutter, A. P. and Schauer, J. J.: The impact of aerosol composition on the particle to gas
793 partitioning of reactive mercury, Environ. Sci. Technol., 41, 3934–3939, doi: 10.1021/es062439i,
794 2007.

Rutter, A. P., Shakya, K. M., Lehr, R., Schauer, J. J., and Griffin, R. J.: Oxidation of gaseous elemental mercury in the presence of secondary organic aerosols, Atmos. Environ., 59, 86–92, 2012.

Saiz-Lopez, A. and von Glasow, R.: Reactive halogen chemistry in the troposphere, Chem. Soc. Rev., 41, 6448–6472, doi: 10.1039/C2CS35208G, 2012.

Saiz-Lopez, A., Shillito, J. A., Coe, H., and Plane, J. M. C.: Measurements and modelling of I_2, IO, OIO, BrO and NO_3 in the mid-latitude marine boundary layer, Atmos. Chem. Phys., 6, 1513–1528, doi:10.5194/acp-6-1513-2006, 2006.

Sander, R., Keene, W. C., Pszenny, A. A. P., Arimoto, R., Ayers, G. P., Baboukas, E., Cainey, J. M., Crutzen, P. J., Duce, R. A., Hönninger, G., Huebert, B. J., Maenhaut, W., Mihalopoulos, N., Turekian, V. C., and Van Dingenen, R.: Inorganic bromine in the marine boundary layer: a critical review, Atmos. Chem. Phys., 3, 1301–1336, doi:10.5194/acp-3-1301-2003, 2003.

Sander, S. P., Abbatt, J., Barker, J. R., Burkholder, J. B., Friedl, R. R., Golden, D. M., Huie, R. E., Kolb, C. E., Kurylo, M. J., Moortgat, G. K., Orkin, V. L., and Wine, P. H.: Chemical Kinetics and Photochemical Data for Use in Atmospheric Studies, Evaluation No. 17, JPL Publication 10-6, Jet Propulsion Laboratory, Pasadena, available at: http://jpldataeval.jpl.nasa.gov, 2011.

Sandu, A. and Sander, R.: Technical note: Simulating chemical systems in Fortran90 and Matlab with the Kinetic PreProcessor KPP-2.1, Atmos. Chem. Phys., 6, 187–195, doi: 10.5194/acp-6-187-2006, 2006.

Schroeder, W. H. and Munthe, J.: Atmospheric mercury – an overview, Atmos. Environ., 32, 809–822, 1998.

Schwartz, S. E.: Mass-transport considerations pertinent to aqueous phase reactions of gases in liquid-water clouds, in: Chemistry of Multiphase Atmospheric Systems, edited by: Jaeschke, D. W., Springer, Berlin, Heidelberg, 415–471, available at: http://link.springer.com/chapter/10.1007/978-3-642-70627-1_16 (last access: 17 April 2015), 1986.

Selin, N. E., Javob, D. J., Park, R. J., Yantosca, R. M., Strode, S., Jaeglé, L., and Jaffe, D.: Chemical cycling and deposition of atmospheric mercury: global constraints from observations, J. Geophys. Res.-Atmos., 112, D02308, doi: 10.1029/2006JD007450, 2007.

Seigneur, C., Wrobel, J. and Constantinou, E.: A chemical kinetic mechanism for atmospheric inorganic mercury, Environmental Science and Technology, 28(9), 1589–1597, 1994.

Shon, Z.-H., Kim, K.-H., Kim, M.-Y., and Lee, M.: Modeling study of reactive gaseous mercury in the urban air, Atmos. Environ., 39, 749–761, 2005.

Sigler, J. M., Mao, H., and Talbot, R.: Gaseous elemental and reactive mercury in Southern New Hampshire, Atmos. Chem. Phys., 9, 1929–1942, doi:10.5194/acp-9-1929-2009, 2009.

Sillman, S., Marsik, F. J., Al-Wali, K. I., Keeler, G. J., and Landis, M. S.: Reactive mercury in the troposphere: model formation and results for Florida, the northeastern United States, and the Atlantic Ocean, J. Geophys. Res.-Atmos., 112, D23305, doi: 10.1029/2006JD008227, 2007.

Simpson, W. R., von Glasow, R., Riedel, K., Anderson, P., Ariya, P., Bottenheim, J., Burrows, J., Carpenter, L. J., Frieß, U., Goodsite, M. E., Heard, D., Hutterli, M., Jacobi, H.-W., Kaleschke, L., Neff, B., Plane, J., Platt, U., Richter, A., Roscoe, H., Sander, R., Shepson, P., Sodeau, J., Steffen, A., Wagner, T., and Wolff, E.: Halogens and their role in polar boundary layer ozone depletion, Atmos. Chem. Phys., 7, 4375–4418, doi:10.5194/acp-7-4375-2007, 2007.

Simpson, W. R., Brown, S. S., Saiz-Lopez, A., Thornton, J. A., and von Glasow, R.: Tropospheric halogen chemistry: sources, cycling, and impacts, Chem. Rev., 115, 4035–4062, doi: 10.1021/cr5006638, 2015.

Snider, G., Raofie, F., and Ariya, P. A.: Effects of relative humidity and CO (g) on the O_3-initiated oxidation reaction of HgO (g): kinetic and product studies, Phys. Chem. Chem. Phys., 10, 5616–5623, 2008.

Soerensen, A. L., Sunderland, E. M., Holmes, C. D., Jacob, D. J., Yantosca, R. M., Skov, H., Christensen, J. H., Strode, S. A., and Mason, R. P.: An improved global model for air–sea exchange of mercury: high concentrations over the North Atlantic, Environ. Sci. Technol., 44, 8574–8580, 2010.

Steffen, A., Douglas, T., Amyot, M., Ariya, P., Aspmo, K., Berg, T., Bottenheim, J., Brooks, S., Cobbett, F., Dastoor, A., Dommergue, A., Ebinghaus, R., Ferrari, C., Gardfeldt, K., Goodsite, M. E., Lean, D., Poulain, A. J., Scherz, C., Skov, H., Sommar, J., and Temme, C.: A synthesis of atmospheric mercury depletion event chemistry in the atmosphere and snow, Atmos. Chem. Phys., 8, 1445–1482, doi:10.5194/acp-8-1445-2008, 2008.

Subir, M., Ariya, P. A., and Dastoor, A. P.: A review of uncertainties in atmospheric modeling of mercury chemistry I. Uncertainties in existing kinetic parameters – fundamental limitations and the importance of heterogeneous chemistry, Atmos. Environ., 45, 5664–5676, 2011.

Talbot, R., Mao, H., and Sive, B.: Diumal characteristics of surface level O_3 and other important trace gases in New England, J. Geophys. Res., 1 10, D09307, doi: 10.1029/2004JD005449, 2005.

Tang, I. N., Tridico, A. C., and Fung, K. H.: Thermodynamic and optical properties of sea salt aerosols, J. Geophys. Res.-Atmos., 102, 23269–23275, 1997.

Tokos, J. J. S., Hall, B., Calhoun, J. A., and Prestbo, E. M.: Homogeneous gas-phase reaction of HgO with H_2O_2, O_3, CH_3I, and $(CH_3)_2S$: implications for atmospheric Hg cycling, Atmos. Environ., 32, 823–827, 1998.

Toyota, K., McConnell, J. C., Staebler, R. M., and Dastoor, A. P.: Air–snowpack exchange of bromine, ozone and mercury in the springtime Arctic simulated by the 1-D model PHANTAS– Part 1: In-snow bromine activation and its impact on ozone, Atmos. Chem. Phys., 14, 4101–4133, doi:10.5194/acp-14-4101-2014, 2014.

866 Verwer, J. G., Spee, E. J., Blom, J. G., and Hundsdorfer, W.: Second-order Rosenbrock method
867 applied to photochemical dispersion problems, SIAM J. Sci. Comput., 20, 1456–1480, 1999.

868 Wang, F., Saiz-Lopez, A., Mahajan, A. S., Gómez Martín, J. C., Armstrong, D., Lemes, M., Hay,
869 T., and Prados-Roman, C.: Enhanced production of oxidized mercury over the tropical Pacific
870 Ocean: a key missing oxidation pathway, Atmos. Chem. Phys., 14, 1323–1335, doi:10.5194/acp-
871 14-1323-2014, 2014.

872 Weiss-Penzias, P., Jaffe, D. A., McClintick, A., Prestbo, E. M. and Landis, M. S.: Gaseous
873 elemental mercury in the marine boundary layer: evidence for rapid removal in anthropogenic
874 pollution, Environ. Sci. Technol., 37(17), 3755–3763, 2003.

875 Xie, Z.-Q., Sander, R., Pöschl, U., and Slemr, F.: Simulation of atmospheric mercury depletion
876 events (AMDEs) during polar springtime using the MECCA box model, Atmos. Chem. Phys., 8,
877 7165–7180, doi: 10.5194/acp-8-7165-2008, 2008.

878 Zhang, L., Wright, L. P., and Blanchard, P.: A review of current knowledge concerning dry
879 deposition of atmospheric mercury, Atmos. Environ., 43, 5853–5864, 2009.

880 Zhang, L., Blanchard, P., Gay, D. A., Prestbo, E. M., Risch, M. R., Johnson, D., Narayan, J.,
881 Zsolway, R., Holsen, T. M., Miller, E. K., Castro, M. S., Graydon, J. A., Louis, V. L. S., and
882 Dalziel, J.: Estimation of speciated and total mercury dry deposition at monitoring locations in
883 eastern and central North America, Atmos. Chem. Phys., 12, 4327–4340, 2012.

884 Table 1. Gas phase Hg reactions in the box model

No.	REACTIONS	KINETIC (cm^{3}molecule^{-1}s^{-1})	REFERENCE
G1	Hg $+ O_3 \rightarrow$ HgO $+ O_2$	$8.43 \times 10^{-17} e^{-1407/T}$	Snider et al., 2008
G2	Hg $+$ OH $\{+O_2\} \rightarrow$ HgO $+$ HO$_2$	$3.55 \times 10^{-14} e^{294/T}$	Pal and Ariya, 2004
G3	Hg $+ H_2O_2 \rightarrow$ Hg(OH)$_2$	8.5×10^{-19}	Tokos et al., 1998
G4	Hg $+$ Cl $\rightarrow$ HgCl	$6.4 \times 10^{-13} e^{(680 \times (1/T - 1/298))}$	Donohoue et al., 2005
G5	Hg $+$ Cl$_2 \rightarrow$ HgCl$_2$	2.6×10^{-18}	Ariya et al., 2002
G6	Hg $+$ Br $\rightarrow$ HgBr	$3.7 \times 10^{-13} (T/298)^{-2.76}$	Goodsite et al., 2004, 2012
G7	Hg $+$ BrO $\rightarrow$ HgBrO	1.8×10^{-14}	Raofie and Ariya, 2004
G8	Hg $+$ I $\rightarrow$ HgI	$4.0 \times 10^{-13} (T/298)^{-2.38}$	Goodsite et al., 2004
G9	HgI $\rightarrow$ Hg $+$ I	$3.0 \times 10^{9} e^{-3742/T}$	Goodsite et al., 2004
G10	HgBr $\rightarrow$ Hg $+$ Br	$1.6 \times 10^{-9} e^{-7801/T} \times [M]$	Dibble et al., 2012
G11	HgBr $+$ Br $\rightarrow$ Hg $+$ Br$_2$	3.89×10^{-11}	Balabanov et al., 2005
G12	HgBr $+$ Br $\rightarrow$ HgBr $+$ Br	3.97×10^{-11}	Balabanov et al., 2005
G13	HgBr $+$ Br $\rightarrow$ HgBr$_2$	2.98×10^{-11}	Balabanov et al., 2005
G14	ClO $+$ HgCl $\rightarrow$ ClHgOCl	5.0×10^{-11}	Dibble et al., 2012
G15	ClO $+$ HgBr $\rightarrow$ BrHgOCl	5.0×10^{-11}	Dibble et al., 2012
G16	BrO $+$ HgCl $\rightarrow$ BrHgOCl	1.09×10^{-10}	Dibble et al., 2012[1]
G17	BrO $+$ HgBr $\rightarrow$ BrHgOBr	1.09×10^{-10}	Dibble et al., 2012; Wang et al., 2014
G18	NO$_2$ $+$ HgCl $\rightarrow$ ClHgNO$_2$	8.6×10^{-11}	Dibble et al., 2012[1]
G19	NO$_2$ $+$ HgBr $\rightarrow$ BrHgNO$_2$	8.6×10^{-11}	Dibble et al., 2012; Wang et al., 2014
G20	HO$_2$ $+$ HgCl $\rightarrow$ ClHgOOH	8.2×10^{-11}	Dibble et al., 2012[1]
G21	HO$_2$ $+$ HgBr $\rightarrow$ BrHgOOH	8.2×10^{-11}	Dibble et al., 2012; Wang et al., 2014
G22	OH $+$ HgCl $\rightarrow$ ClHgOH	6.33×10^{-11}	Dibble et al., 2012[1]
G23	OH $+$ HgBr $\rightarrow$ BrHgOH	6.33×10^{-11}	Dibble et al., 2012; Wang et al., 2014
G24	IO $+$ HgBr $\rightarrow$ BrHgOI	4.9×10^{-11}	Wang et al., 2014

885 [1] The kinetic data of these HgCl reactions were not included in Dibble et al., 2012, they were assumed as the same
886 kinetic as the HgBr reactions, which were calculated by Wang et al. (2014).
887

888 Table 2. Box model input and simulated variables.

Parameter	Appledore Island (AI)	Thompson Farm (TF)	Pack Monadnock (PM)
Observed[1]			
RH, relative humidity	76.9±5.4	69.9±19.5	69.0±13.1
Temperature, °C	19.1±1.7	21.3±4.3	18.5±3.3
[GEM], ppqv	133.9±3.3	138.4±12.8	149.6±3.2
[O$_3$], ppbv	37.4±8.8	32.7±15.7	45.0±4.2
[NO], pptv	154.5[2]	232.4±364.1	85.3±35.8
[CO], ppbv	169.6±13.9	156.2±10.8	120.2±7.2
Simulated[3]			
[Br], ppqv	28.50	0.20	0.18
[OH], ppqv	100.7	75.8	73.5
Other[4]			
v_d, cm s^{-1}, dry deposition velocity	GEM – 0.0045	GEM – 0.07	GEM – 0.08
	GOM – 0.5	GOM – 1.2	GOM – 2.0
	PBM – 0.5	PBM – 0.15	PBM – 0.25
H, M atm^{-1}, Henry's constants	HgO $-$ 3.2×10^9	HgO $-$ 3.2×10^9	HgO $-$ 3.2×10^9
	Hg(OH)$_2$ $-$ 1.2×10^7	Hg(OH)$_2$ $-$ 1.2×10^7	Hg(OH)$_2$ $-$ 1.2×10^7
	Other GOM $-$ 2.7×10^9	Other GOM $-$ 2.7×10^9	Other GOM $-$ 2.7×10^9
L, $m_{water}^3 m_{air}^{-3}$, liquid water content	5×10^{-11}	2.0×10^{-11}	1.25×10^{-11}
D_g, m^{2}s^{-1}, diffusion coefficient	1×10^{-5}	1×10^{-5}	1×10^{-5}
Z, m, boundary layer height	500	200 – 1120[5]	100
r_{dry}, μm, dry aerosol radius	3.5	0.3	0.07

889 [1] Observed 24-h mean values for all studied cases at these sites.
890 [2] Missing NO measurements at AI, use 154.5 ppqv for initial values.
891 [3] Simulated 24-h mean values for all studied days at these sites.
892 [4] Reference: Baumgardner et al., 2000; Kim et al., 2012; Mao and Talbot, 2004; Moldanová and Ljungström, 2001;
893 Pillai and Moorthy, 2001; Shon et al., 2005; Zhang et al., 2009, 2012.
894 [5] TF boundary layer height changed at each hour, the averaged diurnal cycle was obtained from Research Data Archive
895 at the National Center for Atmospheric Research, http://rda.ucar.edu/.
896

897

Table 3. Sensitivity scenarios with varying physical and chemical parameters. The superscript D represents daytime and N nighttime. Downward arrows stand for decreases and upward arrows increases. T stands for the temperature diurnal cycle in the base scenario, and T+10K or T-10K represents 10K higher temperature or 10K lower temperature throughout the day respectively.

| Scenario No. | photolysis | Gas-droplet partitioning | | Rate Coefficients (cm^3 molec^{-1} s^{-1}) | | | Temp. | Results | |
		Include	Liquid water content ($m^3_{water} m^{-3}_{air}$)	GEM+O$_3$ (298K)	GEM+OH (298K)	GEM+Br (298K)		GOM	PBM
Base Scenario									
0	Yes	Yes	5.0E-11	7.5E-19[1]	9.5E-14[2]	3.7E-13[3]	T	--	--
Photochemistry									
1	No	Yes	5.0E-11	7.5E-19	9.5E-14	3.7E-13	T	↓ 3%-92% [D]	↓ 2-100% [D]
Gas-particle partitioning									
2	Yes	No	--	7.5E-19	9.5E-14	3.7E-13	T	↑ ~280%	↓ 100%
Liquid water content									
3	Yes	Yes	3.0E-12	7.5E-19	9.5E-14	3.7E-13	T	↑ ~200%	↓ 80%
4	Yes	Yes	3.0E-10	7.5E-19	9.5E-14	3.7E-13	T	↓ 80%	↑ 50%
Reactions									
5	Yes	Yes	5.0E-11	3.0E-20[4]	9.5E-14	3.7E-13	T	↓ 15% [D] ↓ 85% [N]	↓49% [N]
6	Yes	Yes	5.0E-11	--	9.5E-14	3.7E-13	T	↓ 16% [D] ↓88% [N]	↓ 51% [N]
7	Yes	Yes	5.0E-11	7.5E-19	--	3.7E-13	T	↓ 10% [D]	Negligible
8	Yes	Yes	5.0E-11	7.5E-19	9.5E-14	--	T	↓48% [D]	↓60% [D]
9	Yes	Yes	5.0E-11	7.5E-19	9.5E-14	3.2E-12[5]	T	↑ 250%[D]	↑ 300%
Temperature									
10	Yes	Yes	5.0E-11	7.5E-19	9.5E-14	3.7E-13	T+10K	↓ 9% [D] ↑ 13% [N]	↓ 9% [D] ↑ 54% [N]
11	Yes	Yes	5.0E-11	7.5E-19	9.5E-14	3.7E-13	T-10K	↑ 9% [D] ↓ 11% [N]	↑ 8% [D] ↓ 28% [N]

[1] Snider et al., 2008; [2] Pal and Ariya, 2004; [3] Goodsite et al., 2004, 2012; [4] Hall, 1995; [5] Ariya et al., 2002.

Table 4. Possible pathways of BrO + CH$_3$O$_2$ reaction

NO.	Reactions	Kinetics (cm^{3}molecule^{-1}s^{-1})	Reference
B1	$BrO(g) + CH_3O_2(g) \rightarrow CH_3O(g) + BrOO(g)$ $BrOO(g) \rightarrow Br(g) + O_2(g)$	1.4×10^{-12} Fast	Aranda et al., 1997; Atkinson et al., 2008
B2	$BrO(g) + CH_3O_2(g) \rightarrow CH_2O_2(g) + HOBr(g)$	4.3×10^{-12}	Aranda et al., 1997; Atkinson et al., 2008
B3	$BrO(g) + CH_3O_2(g) \rightarrow CH_3OBr(g) + O_2(g)$	?	Aranda et al., 1997
B4	$BrO(g) + CH_3O_2(g) \rightarrow CH_3OOOBr(g) \rightarrow$ $CH_2O(g) + HOOBr(g)$	?	Guha and Francisco, 2003
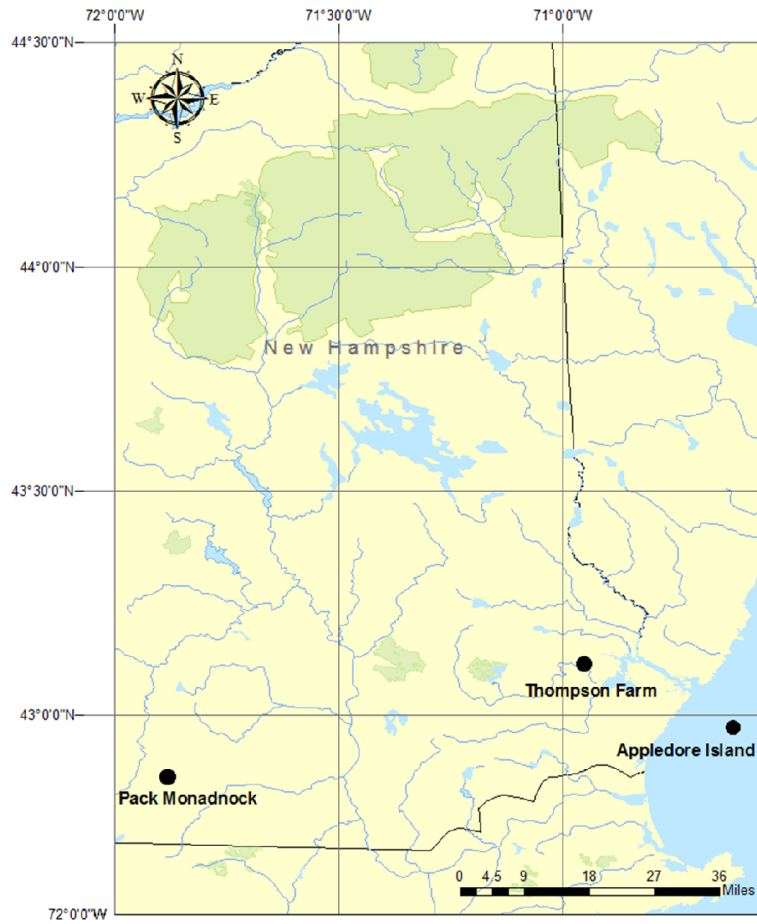
Figure 1. New Hampshire site map: Appledore Island (marine), Thompson Farm (coastal), and Pack Monadnock (inland elevated).
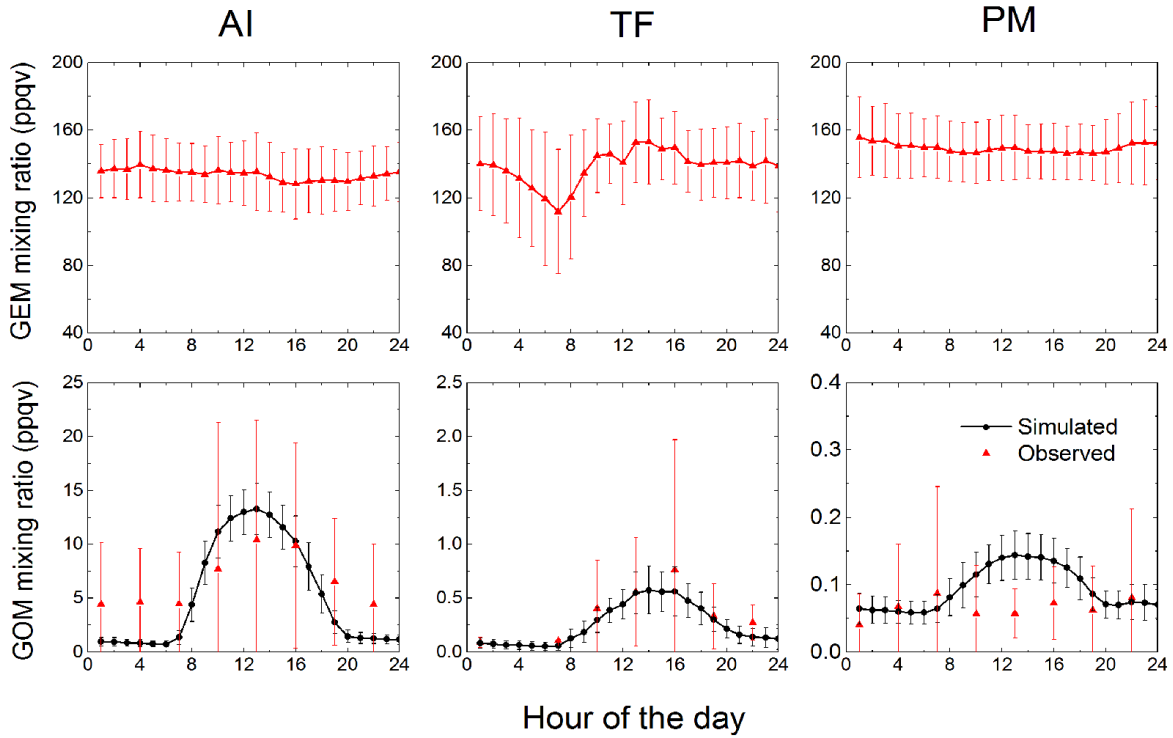
Figure 2. Average diurnal cycles of observed GEM (top panel) and simulated and observed GOM (bottom panel) averaged over the selected 50 days at Appledore Island (AI), 12 days at Thompson Farm (TF), and 21 days at Pack Monadnock (PM) from summers of 2007, 2008, and 2010. The error bars represent standard deviation.
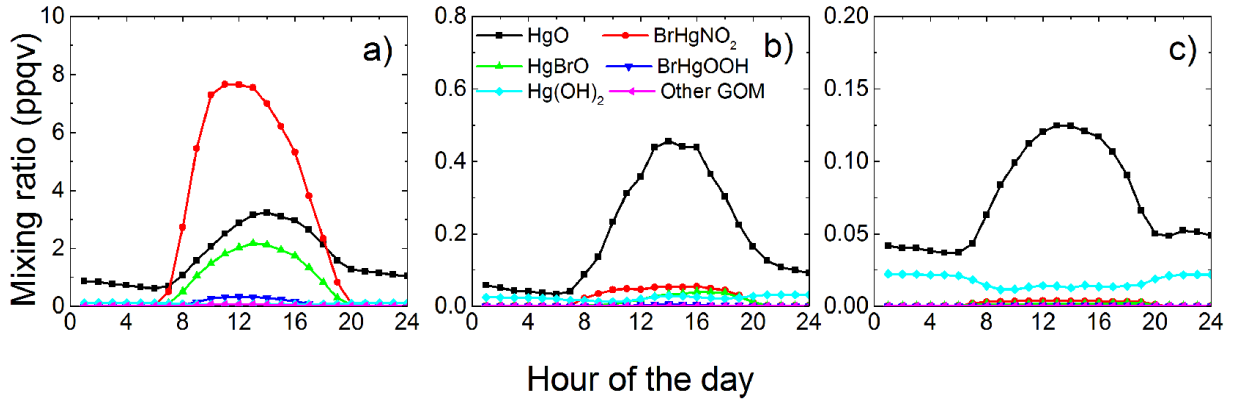
Figure 3. Simulated average diurnal cycles of GOM speciation at AI (a), TF (b), and PM (c).
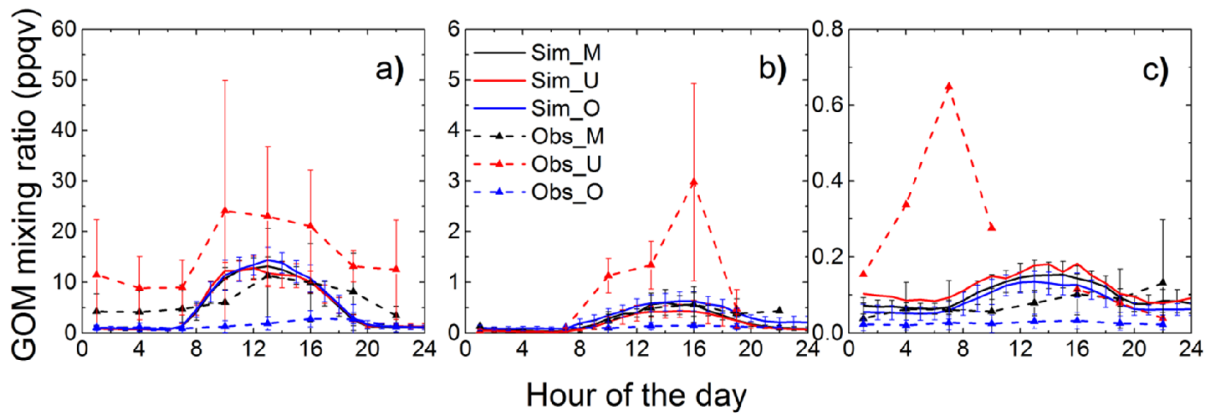
Figure 4. Observed (dash line with scatters) and simulated (solid line) average diurnal cycles of GOM for the matching (black, "Sim_M" and "Obs_M"), under-estimation (red, "Sim_U" and "Obs_U"), and over-estimation cases (blue, "Sim_O" and "Obs_O") at AI (a), TF (b), and PM (c). The bars represent the standard deviations at each hour for those specific days.
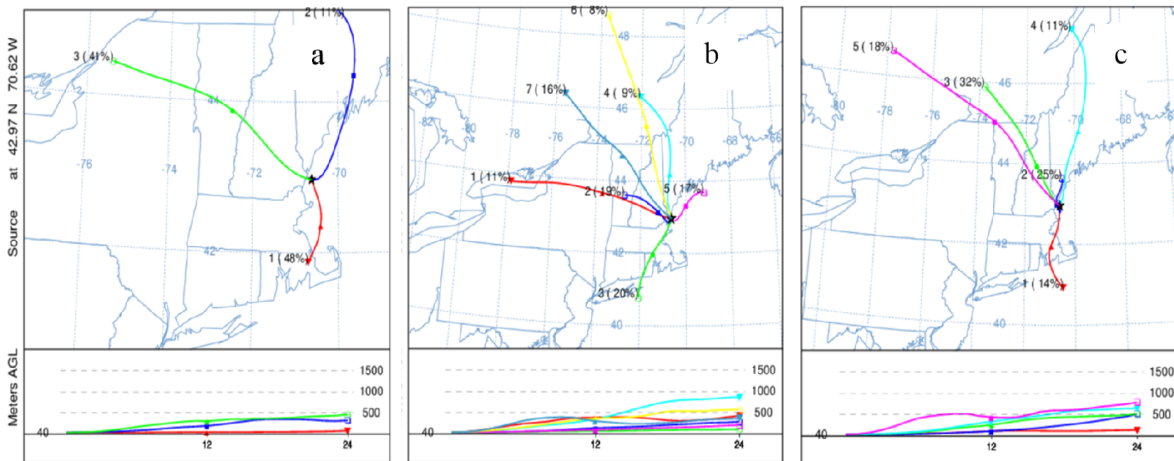
Figure 5. Clustered 24-hours back trajectories of air masses in (a) over-estimation cases, (b) matching cases, and (c) under-estimation cases at AI.
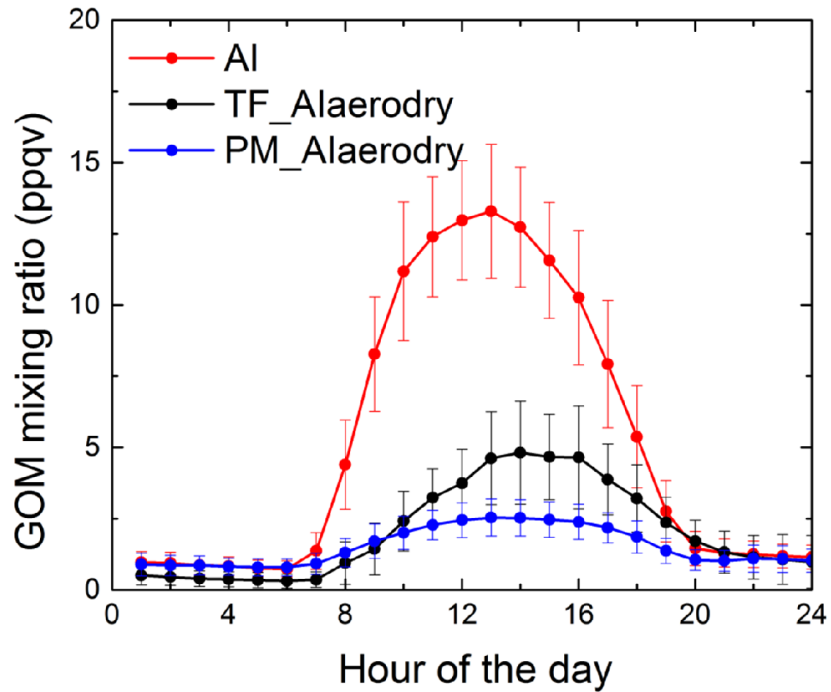
Figure 6. Simulated averaged diurnal cycles of GOM at AI (red), at TF (black) using AI dry deposition and gas-aerosol partitioning parameters ("TF_AIaerodry"), and at PM (blue) using AI dry deposition and gas-to-particle partitioning parameters ("PM_AIaerodry").
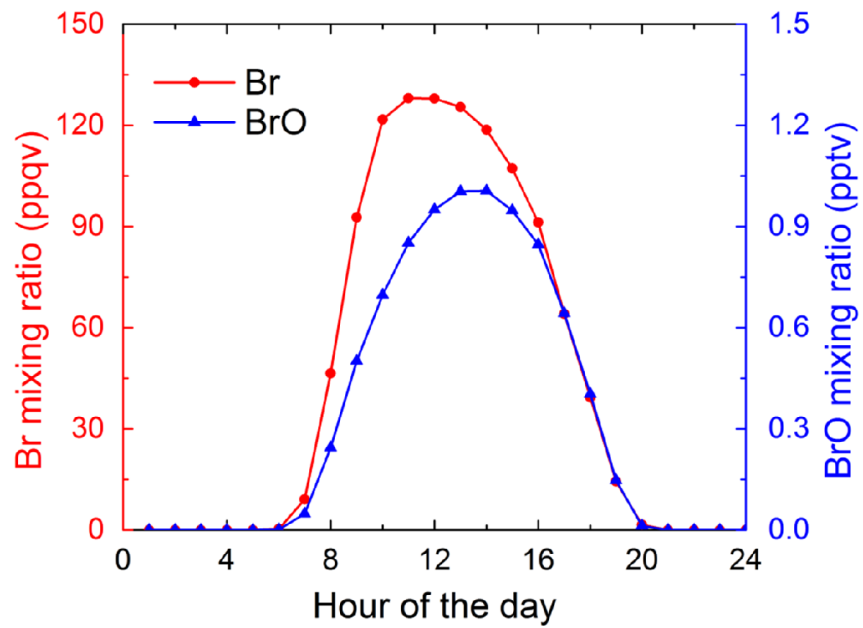
Figure 7. Simulated diurnal cycles of Br (red) and BrO (blue) of the base case.
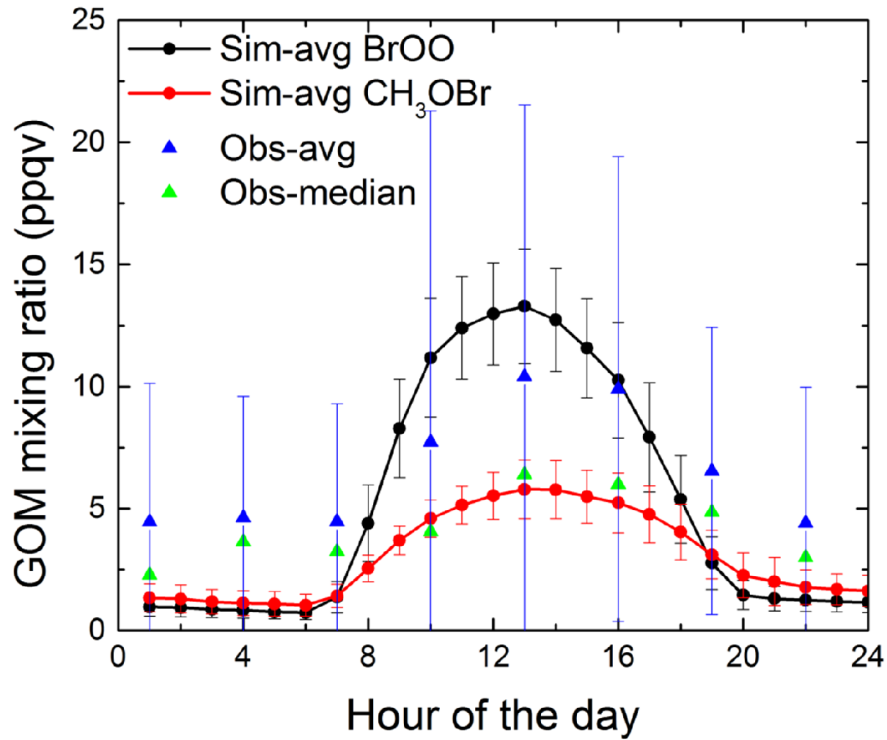
Figure8. Simulated average diurnal cycles of GOM for the base scenario ("Sim-avg BrOO", black circle) and for the "CH_3OBr" scenario ("Sim-avg CH_3OBr", red, circle), observed average GOM diurnal cycle ("Obs-avg", blue, triangle scatter), and observed median GOM diurnal cycle ("Obs-median", green, triangle scatter) of the 50 cases at AI.

Supplement:

Table S1. Aqueous phase reactions and equilibriums of Hg in the box model.

No.	REACTIONS	KINETIC (L mol^{-1} s^{-1}) or EQUILIBRIUM CONSTANT	REFERENCE
A1	Hg^0 (aq) + O_3 (aq) $\rightarrow$ HgO (aq) + O_2 (aq)	2.4×10^9	Munthe et al., 1992
A2	Hg^0 (aq) + OH (aq) $\rightarrow$ HgOH (aq)	2.4×10^9	Gardfeldt et al., 2001
A3	HgOH (aq) + OH (aq) $\rightarrow$ $Hg(OH)_2$ (aq)	1.0×10^{10}	Nazhat and Asmus, 1973
A4	HgOH (aq) + O_2 (aq) + H_2O (aq) $\rightarrow$ $Hg(OH)_2$ (aq) + H^+ + O_2^-	1.0×10^9	Nazhat and Asmus, 1973
A5	Hg^0 (aq) + OH (aq) $\rightarrow$ Hg^+ + OH^-	2.0×10^9	Lin and Pehkonen, 1997
A6	HgO (aq) + H^+ $\rightarrow$ Hg^{2+} + OH^-	1.0×10^{10}	Pleijel and Munthe, 1995
A7	HOCl (aq) + Hg^0 (aq) $\rightarrow$ Hg^{2+} + Cl^- + OH^-	2.09×10^6	Lin and Pehkonen, 1997
A8	ClO^- + Hg^0 (aq) $\rightarrow$ Hg^{2+} + Cl^- + OH^-	1.99×10^6	Lin and Pehkonen, 1997
A9	$HgSO_3$ (aq) $\rightarrow$ Hg^0 (aq) + S(VI)	0.6	Munthe et al., 1991
A10	$Hg(OH)_2$ (aq) $\rightarrow$ Hg^0 (aq) + products	3.0×10^7	Pleijel and Munthe, 1995
A11	Hg^+ + HO_2 (aq) $\rightarrow$ Hg^0 (aq) + O_2 (aq) + H^+	1.0×10^{10}	Xie et al., 2008
A12	Hg^{2+} + HO_2 (aq) $\rightarrow$ Hg^+ + O_2 (aq) + H^+	1.7×10^4	Pehkonen and Lin, 1998
AE1	Hg^{2+} + SO_3^{2-} $\leftrightarrow$ $HgSO_3$ (aq)	2.0×10^{13}	van Loon et al., 2001
AE2	$HgSO_3$ (aq) + SO_3^{2-} $\leftrightarrow$ $Hg(SO_3)_2^{2-}$	1.0×10^{10}	van Loon et al., 2001
AE3	Hg^{2+} + OH^- $\leftrightarrow$ $HgOH^+$	3.98×10^{10}	Smith and Martell, 2004
AE4	$HgOH^+$ + OH^- $\leftrightarrow$ $Hg(OH)_2$ (aq)	1.58×10^{11}	Smith and Martell, 2004
AE5	$HgOH^+$ + Cl^- $\leftrightarrow$ HgOHCl (aq)	2.7×10^7	Xiao, 1994
AE6	Hg^{2+} + Cl^- $\leftrightarrow$ $HgCl^+$	2.0×10^7	Smith and Martell, 2004
AE7	$HgCl^+$ + Cl^- $\leftrightarrow$ $HgCl_2$ (aq)	5.0×10^6	Smith and Martell, 2004
AE8	$HgCl_2$ (aq) + Cl^- $\leftrightarrow$ $HgCl_3^-$	6.7	Smith and Martell, 2004
AE9	$HgCl_3^-$ + Cl^- $\leftrightarrow$ $HgCl_4^{2-}$	13.0	Smith and Martell, 2004
AE10	Hg^{2+} + Br^- $\leftrightarrow$ $HgBr^+$	1.10×10^9	Smith and Martell, 2004
AE11	$HgBr^+$ + Br^- $\leftrightarrow$ $HgBr_2$ (aq)	2.50×10^8	Smith and Martell, 2004
AE12	$HgBr_2$ (aq) + Br^- $\leftrightarrow$ $HgBr_3^-$	1.50×10^2	Smith and Martell, 2004
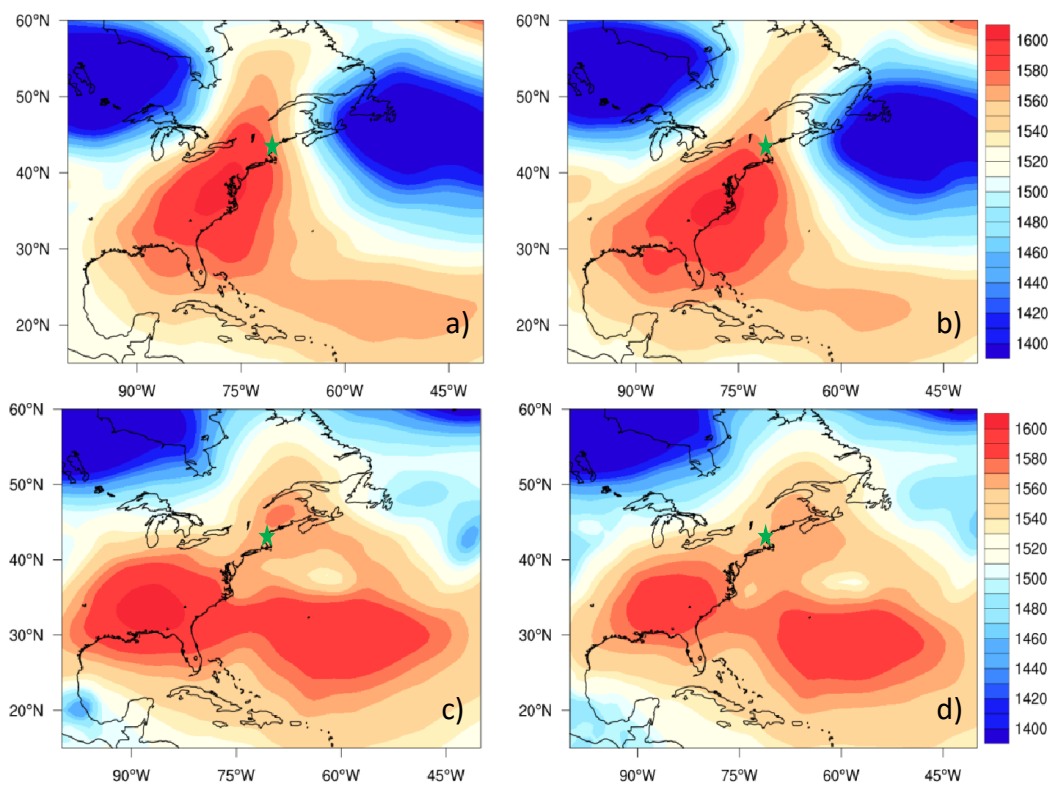
Figure S1. Geopotential height for a) 06/13/2008 08:00 EDT, b) 06/13/2008 14:00 EDT, c) 08/22/2007 14:00 EDT, and d) 08/22/2007 20:00 EDT at 850 hPa, the green star shows the location of TF site.